



Geomorphic and environmental controls on microbial mat fabrics on Little Ambergris Cay, Turks and Caicos Islands

NATHANIEL T. STEIN* , JOHN P. GROTZINGER*, DAVEN P. QUINN†, USHA F. LINGAPPA*, THEODORE M. PRESENT* , ELIZABETH J. TROWER‡, MAYA L. GOMES§, EMILY ORZECOWSKI¶, MARJORIE CANTINE**, KYLE S. METCALFE*, WOODWARD W. FISCHER*, BETHANY L. EHLMANN*, JUSTIN V. STRAUSS†† and ANDREW H. KNOLL‡‡

*Division of Geological and Planetary Sciences, California Institute of Technology, Pasadena, CA 91125, USA (E-mail: nsteingps@gmail.com)

†Department of Geoscience, University of Wisconsin Madison, Madison, WI 53706, USA

‡Department of Geological Sciences, University of Colorado, Boulder, CO 80309, USA

§Department of Earth and Planetary Sciences, Johns Hopkins University, Baltimore, MD 21218, USA

¶Department of Integrative Biology and Museum of Paleontology, University of California, Berkeley, CA 94720, USA

**Department of Earth, Atmospheric and Planetary Sciences, Massachusetts Institute of Technology, Cambridge, MA 02139, USA

††Department of Earth Sciences, Dartmouth College, Hanover, NH 03755, USA

‡‡Department of Organismic and Evolutionary Biology, Harvard University, Cambridge, MA 02138, USA

Associate Editor – Rick Sarg

ABSTRACT

To interpret microbially influenced paleoenvironments in the sedimentary record, it is crucial to understand what processes control the development of microbial mats in modern environments. This article reports results from a multiyear study of Little Ambergris Cay, Turks and Caicos Islands, an uninhabited island floored by broad tracts of well-developed microbial mats on the wind-dominated and wave-dominated Caicos Platform. Uncrewed aerial vehicle-based imaging, differential global positioning system topographic surveys, radiocarbon data, and *in situ* sedimentological and microbial ecological observations were integrated to identify and quantify the environmental factors that influence the distribution and morphologies of Little Ambergris Cay microbial mats, including their response to large storm events. Based on these data, this study proposes that Little Ambergris Cay initially developed from the accretion and rapid lithification of carbonate sediment delivered by converging wave fronts in the lee of adjacent Big Ambergris Cay. Broad tracts of microbial mats developed during late Holocene time as the interior became restricted due to beach ridge development. Minor elevation differences regulate subaerial exposure time and lead to three categories of microbial mats, differentiated by surface texture and morphology: smooth mats, polygonal mats and blister mats. The surface texture and morphology of the mats is controlled by subaerial exposure time. In addition to elevation, the spatial distribution of mats is largely controlled by hydrodynamics and sediment transport during large storm events. This detailed assessment of the controls on mat formation and preservation at Little Ambergris Cay provides a framework within which to identify and understand the interactions between microbial communities and sediment transport processes in ancient high-energy carbonate depositional systems.

Keywords Carbonate platform, drone remote sensing, hyperspectral imaging, microbial mats, microbial sedimentary fabrics, Turks and Caicos.

INTRODUCTION

Sedimentary fabrics interpreted to result from the interaction of microbial communities with carbonate sediments and cements are ubiquitous in the rock record; such fabrics comprise major components of Precambrian carbonate platforms (Walter *et al.*, 1976; Grotzinger, 1989). Stromatolites – “laminated, lithified sedimentary growth structures, accretionary away from a point or limited surface of initiation” (Semikhatov *et al.*, 1979) – occur in the rock record since early Archean time and have long been targets for the study of the fossil record of ancient life (Grotzinger & Knoll, 1999; Schopf, 2006; Allwood *et al.*, 2009; Knoll, 2015). Modern stromatolites are restricted to relatively rare occurrences (e.g. Logan, 1961; Dravis, 1983; Dill *et al.*, 1986; Reid *et al.*, 1995), but flat laminated microbial mats and the sedimentary structures they form are more widely distributed and carry equal significance in the documentation and interpretation of Earth history (Schopf, 2006; Grotzinger & Al-Rawahi, 2014). This makes them a promising target for modern analogue studies.

Microbial mats display a wide array of surface morphologies and yield distinctive sedimentary structures and textures that arise syndepositionally from the interaction of mats and biofilms with environmental factors such as desiccation, hydrodynamics (forces from water flow, particularly during storms) and physical sediment dynamics (Gerdes *et al.*, 2000; Schieber *et al.*, 2007; Noffke, 2010; Grotzinger & Al-Rawahi, 2014). Such textures may be preserved in the rock record, often as topographic features on bedding planes that hosted ancient microbial mats (Schieber *et al.*, 2007; Noffke, 2010). In the absence of lithified stromatolitic structures, evidence of ancient mats commonly relies on mineral and organic content in adjacent laminae (e.g. Allwood *et al.*, 2009), the presence of disseminated stratiform pyrite (Pflüger & Gresse, 1996) or various geochemical signatures (e.g. Marshall *et al.*, 2007; Bontognali *et al.*, 2012). In some cases, early diagenetic silicification also preserves mat building populations (e.g. Knoll *et al.*, 2013). Collectively, microbial mats and their associated sedimentary structures in modern environments are studied as process analogues for

similar structures in the rock record (e.g. Dupraz *et al.*, 2009).

To aid interpretation of microbially influenced textures in the sedimentary carbonate record, it is crucial to understand what processes determine the surface morphology of modern microbial mats and document the range of these textures in carbonate sediments. Several processes are hypothesized: (i) microbial community composition (Golubic, 1991; Visscher *et al.*, 1998; Dupraz & Visscher, 2005; Shepard & Sumner, 2010); (ii) ecological succession and the developmental trajectory of mats towards increasing morphological and compositional complexity (Reid *et al.*, 2000); and (iii) physical environmental factors such as hydrodynamics, sedimentation, subaerial exposure, temperature and insolation (Gebelein, 1969; Wanless *et al.*, 1988; Martin *et al.*, 1993; Andres & Reid, 2006; Noffke *et al.*, 2013; Mariotti *et al.*, 2014; Trembath-Reichert *et al.*, 2016; Wu *et al.*, 2021).

Microbial mats are relatively uncommon in modern shallow or deep marine facies due to ecological restriction resulting from competition with other organisms and from animal grazing and bioturbation. Additionally, local environmental factors such as temperature, oxygen and light availability, and the energy of the depositional environment can impact the distribution of microbial mats. This study focused on microbial mats developed on parts of Little Ambergris Cay, located on the Caicos Platform, a wind-wave-dominated high energy environment (Fig. 1; Wanless *et al.*, 1989; Dravis & Wanless, 2017) subject to frequent storms. Microbial mats in modern carbonate tidal environments are often grouped into two morphological classes: flat laminar mats and domical ‘biscuit’ mats (e.g. Wanless *et al.*, 1988; Golubic, 1991). Following Hurricane Kate in 1985, Wanless *et al.* (1988) postulated that these morphotypes observed on West Caicos formed from cyanobacteria that colonize the substrate at different rates: *Schizothrix* rapidly colonizes and stabilizes overlying sediment to form flat mats that inhibit desiccation structures, and *Scytonema* colonizes more slowly to form mats marked by raised desiccation polygons. Subsequent microscopic and genomic studies of flat and domical

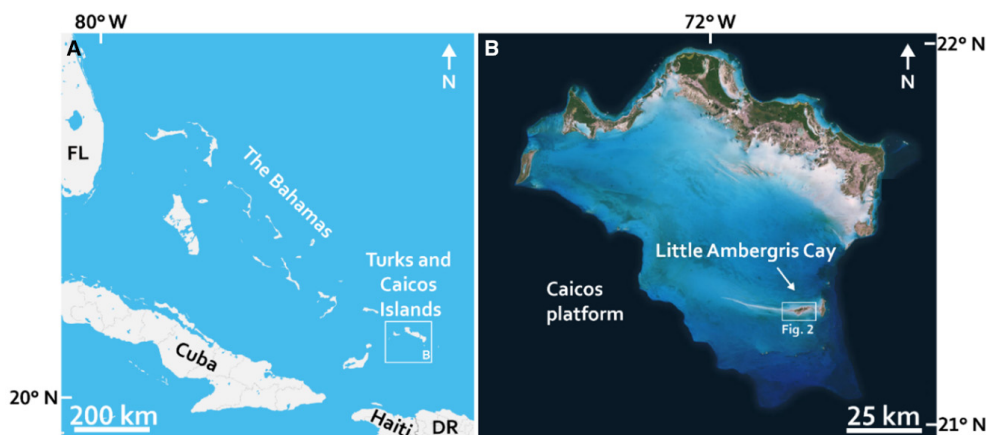


Fig. 1. (A) Location of the Turks and Caicos Islands. (B) Satellite perspective of the Caicos Platform. Little Ambergris Cay is shown in the white box. Image procured using QGIS OpenLayers plugin.

mats on Little Ambergris Cay revealed that although surface layer cyanobacterial populations are responsible for much of the mat's structure, populations of *Schizothrix* and *Scytonema* are indistinguishable between mat morphotypes (Trembath-Reichert *et al.*, 2016). Instead, Trembath-Reichert *et al.* (2016) proposed that the microbial mat morphology is controlled principally by the response of microbial communities to environmental factors like exposure and sedimentation. Wu *et al.* (2021) similarly identified changes in the expression and distribution of microbial mats in response to sea-level oscillations on Andros Island.

The role of specific environmental factors in the formation and development of microbial mats has been recognized (Gebelein, 1969; Martin *et al.*, 1993; Andres & Reid, 2006; Mariotti *et al.*, 2014; Trembath-Reichert *et al.*, 2016; Wu *et al.*, 2021). However, knowledge of the sedimentological and geomorphological factors that impact the distribution of mat morphotypes on carbonate platforms is necessary to interpret variations in modern and ancient microbial mat morphologies. The present study integrated *in situ* and uncrewed aerial vehicle (UAV)-based observations with radiocarbon data from carbonate sediments on Little Ambergris Cay over several field sessions to identify and quantify the sedimentological, geomorphological and environmental factors that influence the texture and distribution of its microbial mats, including water depth, subaerial exposure time and sediment flux during storm events. These results allow insights into the development and history of microbial mats on Little Ambergris Cay over the course of the island's evolution.

GEOLOGICAL SETTING

The Caicos Platform sits near the southern limit of Bahamian platform complexes (Fig. 1). The platform is approximately 100 km north–south and 70 km east–west and lies between 71°30' and 72°30'W and 21° and 22°N. The platform is subject to stronger easterly trade winds than the northern Bahamian platforms (Dravis & Wanless, 2017), with typical wind velocities of $8.1 \pm 2.6 \text{ m s}^{-1}$ (Trower *et al.*, 2018). Wind–wave agitation promotes formation and transport of oolitic sands across the platform interior (Dravis & Wanless, 2017; Trower *et al.*, 2018). Powerful storms also are common; on average Little Ambergris Cay experiences hurricane-force winds every five and a half years (Landsea & Franklin, 2013). The Caicos Platform has a subarid climate, averaging 50 to 70 cm year⁻¹ of precipitation and temperatures of 20 to 25°C (NOAA/NOS/CO-OPS). The tidal range is >1 m and tides are semi-diurnal (Dravis & Wanless, 2017). A string of islands cored by Pleistocene bedrock dominates the north-western, northern and north-eastern platform margins, having formed during multiple periods of Pleistocene sea-level oscillation (Wanless *et al.*, 1989; Kerans *et al.*, 2019).

Little Ambergris Cay physiography

Little Ambergris Cay is about 6.5 km long, 1.6 km wide, and 6.1 km². It is an uninhabited island near the southern margin of the Caicos Platform (Figs 1 and 2). The cay sits where oolitic sediments transported in easterly trade wind-driven currents converge in the lee of Big Ambergris Cay to form a linear, shallow subtidal shoal



Fig. 2. Orthomosaic of Little Ambergris Cay produced in July 2016 using a DJI Phantom 4 Pro uncrewed aerial vehicle (UAV) with a 12-megapixel camera. More than 1500 RGB images were collected during 13 separate flights over seven days, yielding 13.1 cm pixel⁻¹ resolution. Photogrammetry was conducted in Agisoft Photoscan. White streaks represent specular reflection of sunlight on shallow water. The images are not radiometrically corrected. Locations of vibracore measurements (Fig. 17) and tide gauge measurements (Fig. 3C) are shown.

extending *ca* 20 km westward (Wanless *et al.*, 1989; Dravis & Wanless, 2008, 2017; Trower *et al.*, 2018). Partially lithified upper shoreface to aeolian skeletal–oolitic grainstone and intraclasts form *ca* 1.0 to 4.5 m high Holocene ridges that surround an extensive interior basin with peritidal water depths. Daily tides flood the interior to shallow water depths averaging <1 m.

The interior of the cay is floored by broad tracts of well-developed microbial mats interspersed with mangroves (predominantly *Rhizophora mangle*), ooid hardgrounds, and ooid grainstones and scrubland. The north-western portion of the cay is covered with a network of mangroves floored by well-developed, polygonal, tufted filamentous mats. Most of the interior basin is covered by microbial mats with varying morphologies (see *Surface sedimentology and microbial mat descriptions* section) interspersed with exposed *in situ* ooid hardgrounds. A series of active channels connects tidal inlets on the north and south sides of the island.

METHODS

This study was conducted over six field sessions: (i) June to July 2016 (10 days); (ii) August 2017 (10 days); (iii) September 2017 (one day); (iv)

March 2018 (four days); (v) July 2018 (four days); and (vi) July 2019 (four days). The last four field sessions followed Hurricane Irma, which directly impacted Little Ambergris Cay on 7 September 2017 as a Category 5 hurricane. Study methods included UAV-based imaging, ground-based topographic surveying, tidal range monitoring, coring of subsurface geology, radiocarbon dating of shell material, and surface geological mapping of sedimentary structures and microbial mat morphology and distribution.

Uncrewed aerial vehicle imaging

Orthomosaics and digital elevation models (DEMs) of Little Ambergris Cay were generated in July of 2016 and 2017 using RGB images collected with a DJI Phantom-4 Pro (DJI, Shenzhen, China). Photogrammetry and mosaic generation were performed using Agisoft Photoscan software. The 2016 full-island orthomosaic (Fig. 2) was collected during manual flights at 250 m altitude. More than 1500 overlapping, 12-megapixel images were taken with a nadir-looking camera at a spatial resolution of 13.8 cm pixel⁻¹. A DEM (Fig. 3A) was created from the 2016 images.

More than 20 ground control points (GCPs) were generated with a differential global positioning system (DGPS) unit across the island (*Geological topographic survey and mapping of sediment*

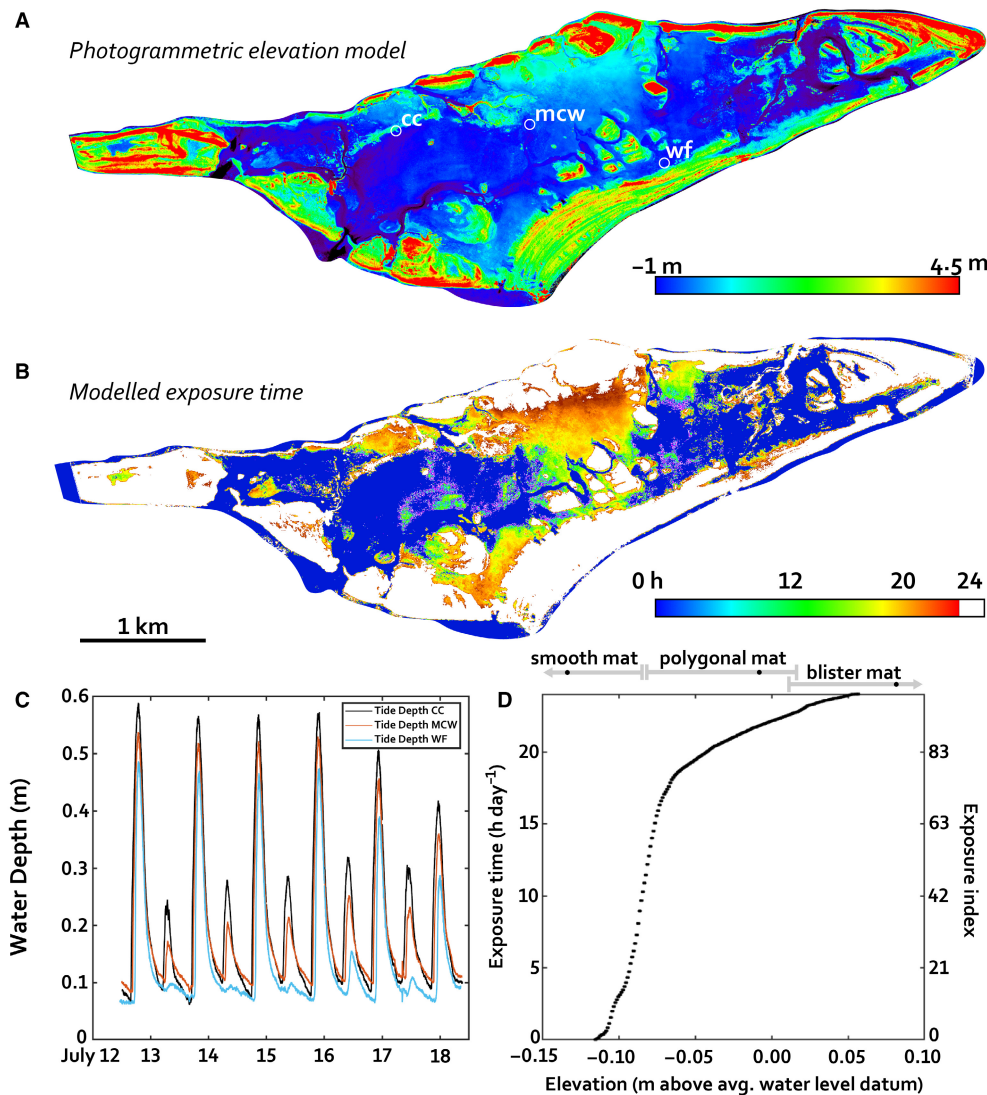


Fig. 3. (A) Elevation model of Little Ambergis Cay made in July 2016 by combining more than 1500 RGB images collected over 13 separate flights with a DJI Phantom 4 Pro with a 12-megapixel camera. Generated in Agisoft Photoscan. (B) Map of average number of hours per day that the surface is exposed. Calculated using a spatially weighted average of tide data from three locations on the island (C) and the elevation model in (A). (C) Tide data collected at three sites over six days during July 2018. Measurement locations are shown in Fig. 2. (D) Comparison of modelled exposure time (hours per day) and elevation relative to the average water level datum. All digital elevation model (DEM) points are sampled. The range capturing 95% of elevations for smooth mats, polygonal mats and blister mats and their DEM-derived mean elevation (black dot) is shown above the plot.

types section). Long-wavelength DEM distortion from image alignment errors was corrected by fitting a three-dimensional polynomial to the down-sampled DEM and subtracting it from the original DEM to minimize error relative to *in situ* survey points (Fig. 4A and B). The resulting DEM was referenced so that an elevation of 0 m is the mean water level (MWL) observed between three tide gauge sites over six days during July 2018 (*Tidal*

range measurements and exposure time modelling section; Fig. 3C).

Hyperspectral images of the interior basin were taken with a Headwall Nano-Hyperspec Visible and Near Infrared pushbroom imaging spectrometer (Headwall Photonics, Bolton, MA, USA), which captures 276 spectral bands between 400 to 1000 nm. Images were collected during 20 drone flights in August 2017 and March 2018 in

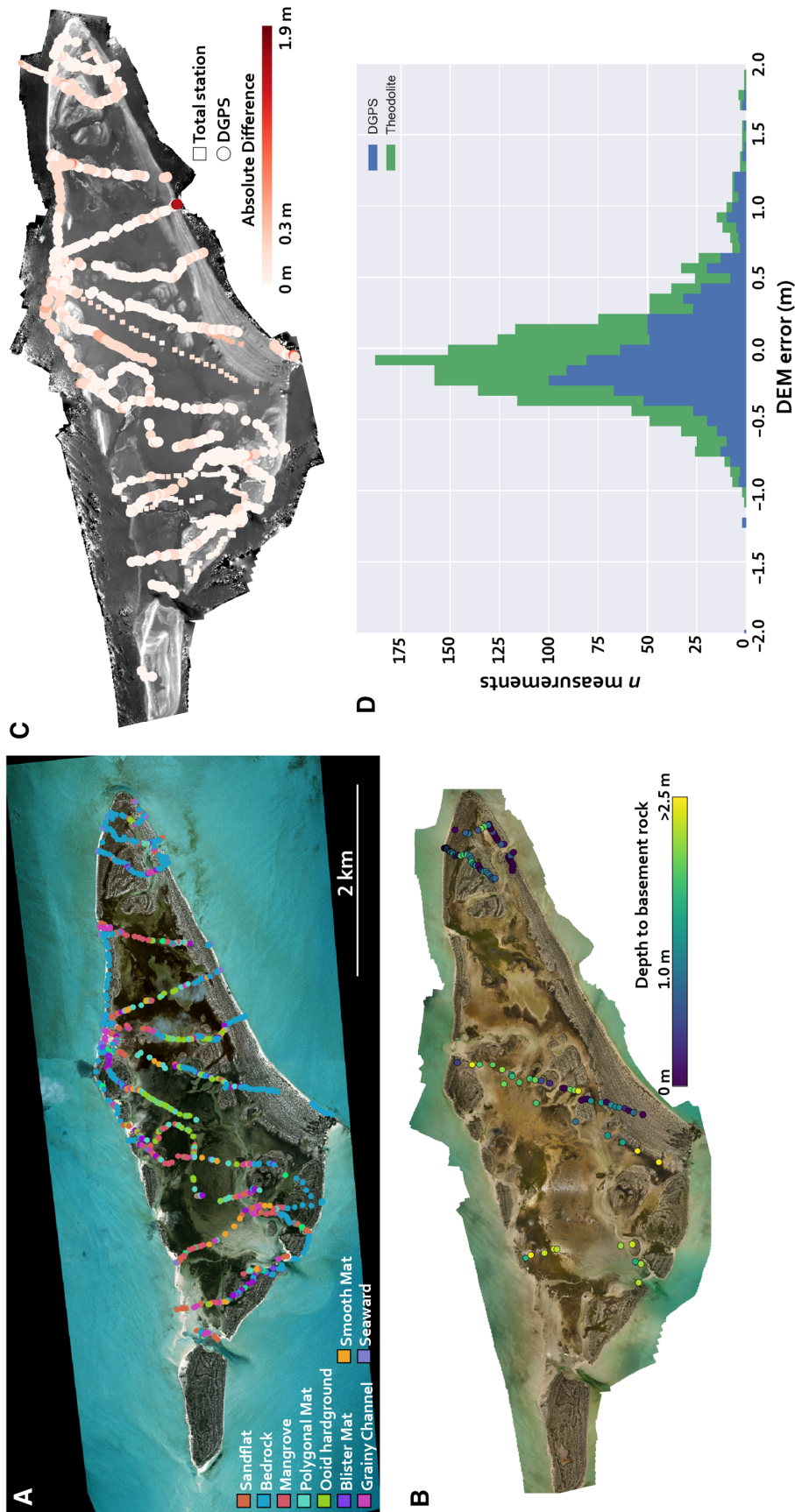


Fig. 4. (A) Classification of sediment types during ten transects of Little Ambergris Cay. Sediment types were classified *in situ* and positions were marked with a differential global positioning system (DGPS). (B) Depth to basement rock relative to surface elevation. Measured at 127 sites using a 1 cm diameter, 2.5 m long stainless-steel rod. (C) Absolute elevation difference between the 2016 photogrammetric digital elevation model (DEM) and total station and DGPS elevation survey points. (D) Histogram showing the distribution of DEM errors.

variable lighting conditions. The sensor has 640 pixels and a 50.7° angular field of view, yielding *ca* 20 cm resolution from 100 m elevation. The camera was mounted on a DJI Ronin-MX 3-axis gimbal on a DJI Matrice 600 Pro UAV. Flights were automated with DroneDeploy software to fly at constant speed to match the static frame rate of the spectrometer. Reflectance R was calculated for each image pixel, i , as:

$$R_i = \frac{R_{\text{cal}}(W_i - D_i)}{W_{\text{cal}} - D_i} \quad (1)$$

where W is the detector digital number, D is the dark current measured prior to flight, W_{cal} is the digital number averaged from the brightest non-saturated shade of a 10' × 10' calibration target placed in the scene, and R_{cal} is the lab-measured reflectance of the calibration target. The resulting product was a set of $n \times 640 \times 276$ reflectance image cubes that were corrected for atmospheric absorption and illumination assuming homogeneous atmospheric conditions and illumination across each scene, where n is the number of pixel rows in the direction of flight. The images were not orthorectified because there is little topographic relief in the interior basin. Rows of each reflectance cube were independently georeferenced by extracting the GPS-based camera position and correcting for variations in UAV altitude, heading and speed. The rows were then stitched into a single mosaic and warped to GCPs manually selected from the colour orthomosaic. Maps of the absorption band depths of reflectance features corresponding to different characteristic microbial pigments present in the mats, including phycobilins (590 nm), phycocyanin (620 nm), chlorophyll *a* (680 nm), bacteriochlorophyll *c* and/or *d* (720 nm) and bacteriochlorophyll *a* (800–890 nm), were calculated from these cubes (Fig. 5) (features described in Hubas *et al.*, 2011).

Geological topographic survey and mapping of sediment types

During June–July 2016 and August 2017, a high-precision elevation survey was conducted using point measurements from a Total Station electronic transit theodolite and Septentrio DGPS system (Septentrio, Leuven, Belgium). 847 DGPS elevation and sediment type survey points (Fig. 4A) and 1334 total station elevation points (Fig. 4C) were collected during island transects. As with the DEM, all DGPS and total station elevation data were offset with the MWL at 0 m elevation.

A subset of elevation survey points was used as GCPs for the DEM (*Uncrewed aerial vehicle imaging* section) and the remaining points were used to validate DEM accuracy and assess sediment type elevation. Comparison of *in situ* elevation survey points with the DEM shows absolute elevation differences of <0.1 m for *ca* 75% of interior points (Fig. 4C and D), indicating that the DEM is approximately representative of true elevations. Most larger elevation deviations are in vegetated areas where plant canopies can skew photogrammetric elevations.

An island-wide pre-Hurricane Irma map of sediment types (Fig. 6) was drafted using the 2016 UAV orthomosaic augmented with sediment type identifications made during island transects. Violin plots of the sediment type elevation distribution were generated by extracting the elevation of each sediment type map pixel from the 2016 DEM and comparing it to the sediment type elevations extracted from DGPS measurements (Fig. 7, Table 1). Violin width was normalized to the sample count of each sediment type. Long-tailed elevation distributions are potentially attributable to four factors: (i) elevation errors in the DEM; (ii) systemic DEM error caused by the polynomial surface warping correction; (iii) errors in the sediment type map; and (iv) true physical elevation variation. Sporadic DEM errors, coupled with the relatively low vertical resolution, produce significant point-to-point elevation variability that contributes to artificially long-tailed elevation distributions. Because the number of points sampled per sediment type is high (>4.3e6, Table 1), the mean DEM-derived elevation is likely close to the true mean elevation if the elevations are not shifted by spatially asymmetrical warping. The consistently low absolute elevation differences between the DEM and *in situ* elevation survey points (Fig. 4B) indicate that the DEM is not significantly warped. Misidentification of microbial mats in the UAV orthomosaic due to surface colour similarities could artificially increase their elevation overlap. The range of sediment type elevations from DGPS points is more accurate than the photogrammetric DEM due to the higher vertical resolution and *in situ* sediment type assignments (Fig. 7).

Tidal range measurements and exposure time modelling

Tidal water depth variations in the island interior were measured at three sites in July 2018 with HOBO U20L water depth loggers (Fig. 3C;

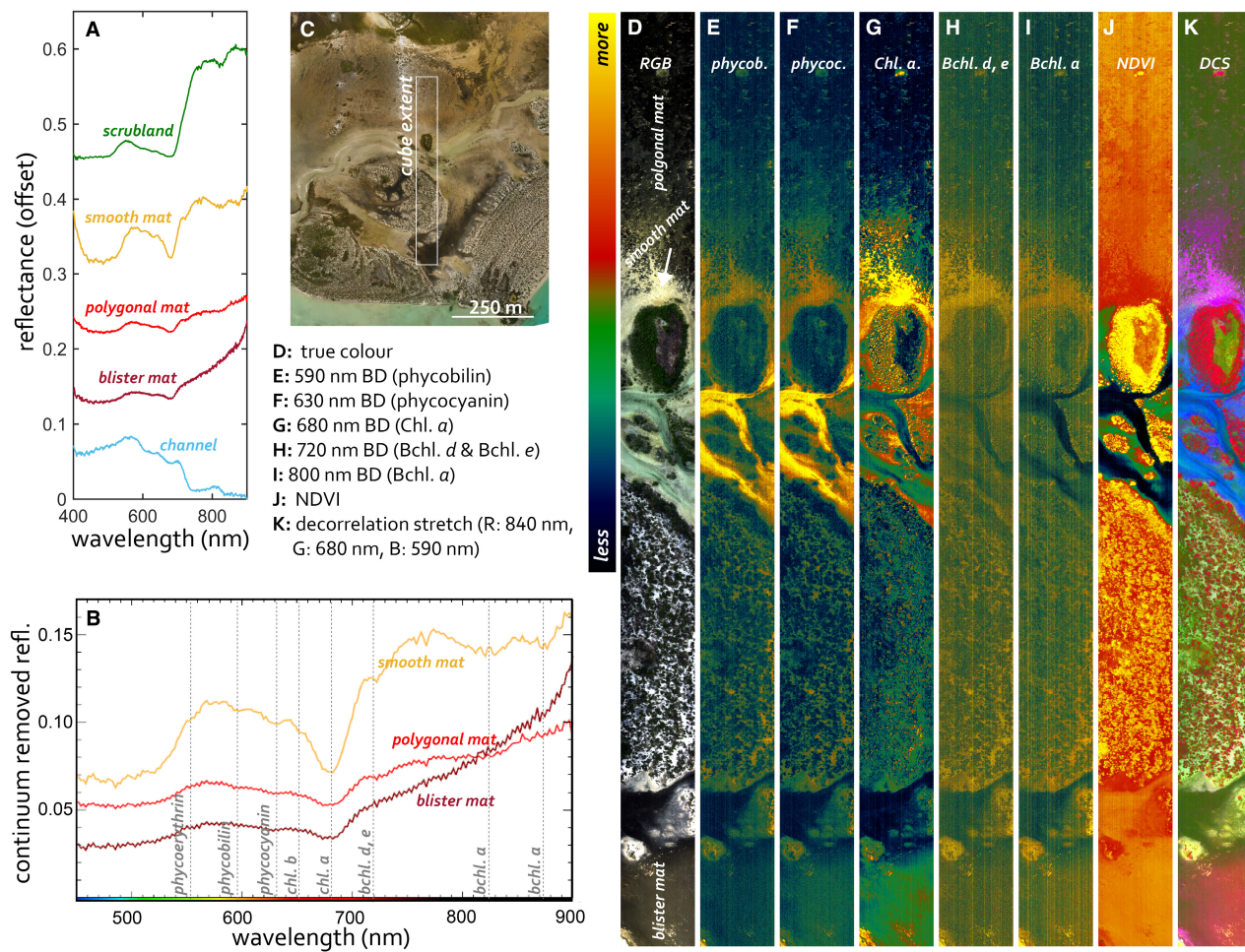


Fig. 5. (A) Averaged overhead reflectance spectra of scrubland, smooth mat, polygonal mat, blister mat and a channel. (B) Continuum removed spectra of the mats (A) with major pigment absorption features labelled. (C) Extent of representative hyperspectral image shown in (D) to (K). (D) Approximate true colour image of scene with each mat morphotype. (E) Phycobilin absorption depth. (F) Phycocyanin absorption depth. (G) Chlorophyll *a* absorption depth. (H) Bchl. *d* and *e* absorption depth. (I) Bchl. *a* absorption depth. (J) Normalized difference vegetation index. (K) Decorrelation stretch (R: 840 nm, G: 680 nm, B: 590 nm).

Tempcon Instrumentation Limited, Arundel, UK). Water depths were calculated assuming seawater density and using a local barometric pressure correction from a HOBO U20-001-01-Ti logger mounted on a beach ridge. The mean water level across the interior was estimated by calculating a temporal average of the water depth at the logging sites, offset by DEM-measured surface elevation, assuming insignificant tidal lag between their separation distances of 0.8 km, 0.9 km, and 1.7 km. It should be noted that the water level may vary seasonally.

Exposure index – the percentage of time that a given point is exposed above water level (Ginsburg *et al.*, 1977) – was calculated from daily

exposure time maps generated using the DEM and tidal range measurements. A 13.1 cm/pixel grid was populated in ten-minute time steps with the distance-weighted average of water depths measured at the logging sites, offset for local elevation sourced from the DEM. The resulting rasters were time-averaged to calculate the average daily exposure index across the island (Fig. 3B). Exposure index and elevation values were plotted for every point on the island (Fig. 3D). The range of exposure indices encapsulating 95% of the points measured for each mat type was calculated from this curve using the DEM-based mean mat elevations and DGPS-based elevation ranges (Fig. 7).

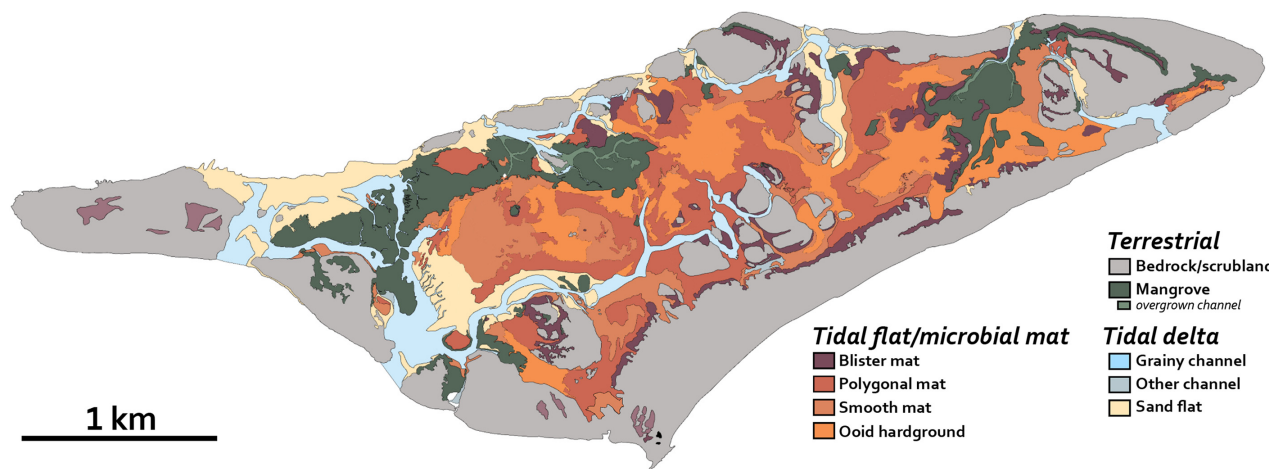


Fig. 6. Pre-Irma sediment type map of Little Ambergris Cay generated by mapping onto the $13.8 \text{ cm pixel}^{-1}$ orthomosaic in Fig. 2 and using the differential global positioning system (DGPS) transect classifications shown in Fig. 4A.

Depth to bedrock and sediment coring

A 1 cm diameter, 2.5 m long stainless-steel sediment probe was used to measure the depth to impassably hard material (possibly Holocene oolitic grainstone) at 127 sites (Fig. 4B). Bedrock depths sometimes exceeded the 2.5 m probe length. Sediment vibracores were obtained by clamping 10' core barrels (3" outer diameter, 0.083" wall thickness aluminium 6063) to a concrete vibrator driven by a portable motor. The vibrating barrels were sunk into the sediment using guide ropes tied to the top of the barrel and sealed with a 3" plug before recovery. Core compaction and recovery were calculated from measurements of core barrel penetration, depth of core top prior to plug emplacement, and recovered sediment length. Compaction ranged between 11 to 18% for the cores shown. The barrels and core were split with a circular saw and wire, respectively. A portion of a core suspected to contain relict mat material was imaged with a Headwall Nano-Hyperspec VNIR imaging spectrometer (*Uncrewed aerial vehicle imaging section*) using a Thorlabs KMTS50E translation stage (Thorlabs Inc., Newton, NJ, USA).

Radiocarbon dating

Strombus (conch) and bivalve fragments were sampled from three cores and multiple outcrops along the island's lithified rim for radiocarbon dating (Fig. 2). The samples were leached with

dilute hydrochloric acid prior to hydrolysis with 85% phosphoric acid. Analyses were performed at the University of California Irvine Keck Carbon Cycle AMS Facility. Radiocarbon concentrations are given as fractions of the modern standard, $\Delta^{14}\text{C}$, and conventional radiocarbon age following the convention of Stuiver & Polach (1977) (Table 2). Sample preparation backgrounds were subtracted based on measurements of ^{14}C -free calcite. All results were corrected for isotopic fractionation following Stuiver & Polach (1977) with $\delta^{13}\text{C}$ values measured on prepared graphite using an AMS spectrometer.

RESULTS

Surface sedimentology and microbial mat descriptions

Eight surface sediment types and biotic elements were identified across the island including: beach ridge rim with scrubland, sand flats, channels, ooid hardground-floored bay, mangroves, smooth mats, polygonal mats and blister mats. Most of these occur within an overlapping range of elevations (Fig. 7), leading to lateral equivalence of some components.

Carbonate sediment types that comprise the beach ridge rim are dominated by fossiliferous and oolitic grainstone and coarse intraclasts that are characterized by seaward-dipping low angle stratification, large irregular pores, fossiliferous

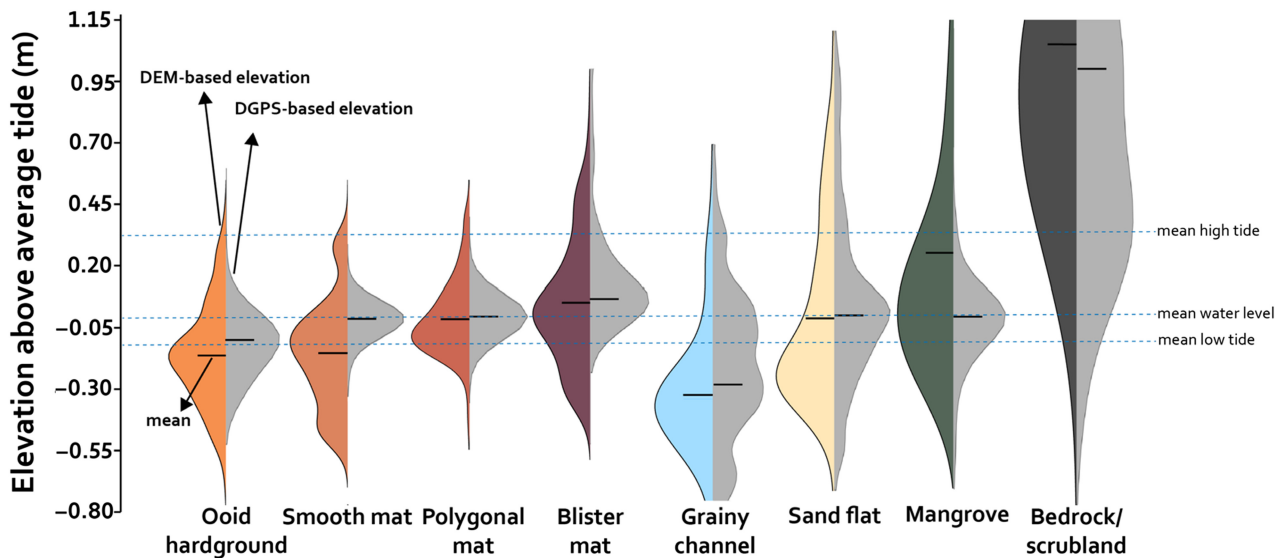


Fig. 7. Violin plot of the elevations of the sediment types. Elevations on the left side of each violin are sourced from the 2016 uncrewed aerial vehicle (UAV)-based digital elevation model (Fig. 3A) and sediment types are sourced from the corresponding sediment type map (Fig. 6). Elevations on the right side of each violin are sourced from the differential global positioning system (DGPS) data shown in Fig. 4A. Elevations are relative to the average water level (0 m). Plot width denotes the relative abundance of each sediment type at a particular elevation.

Table 1. Elevation and exposure statistics of all sediment types on Little Ambergis Cay.

Facies	Number of pixels in facies map	Area (km ²)	Mean DEM elevation (m rel. mean water level)	Standard deviation DEM elevation	Standard error DEM elevation	Median DEM elevation (m rel. mean water level)	Number of DGPS measurements	Median DGPS elevation (m rel. mean water level)
Ooid hardground	5 611 982	0.48	-0.152	0.227	9.6e-5	-0.162	75	-0.12
Smooth mat	4 713 509	0.41	-0.144	0.221	1.0e-4	-0.137	35	-0.02
Polygonal mat	8 823 409	0.76	-0.008	0.160	5.4e-5	-0.037	72	0.00
Blister mat	4 307 242	0.37	0.062	0.277	1.3e-4	0.036	60	0.08
Grainy channel	5 661 462	0.49	-0.327	0.315	1.3e-4	-0.346	106	-0.29
Sand flat	4 799 307	0.41	0.005	0.391	1.8e-4	-0.118	75	0.00
Mangrove	7 673 826	0.66	0.265	0.620	2.2e-4	0.107	98	-0.02
Bedrock	29 300 125	2.53	1.109	0.802	1.5e-5	0.788	326	1.07

lags, imbricated beachrock boulders, high-angle trough cross-bedding and variable bioturbation. Much of the bedrock rim reaches *ca* 1.0 to 4.5 m above MWL (Fig. 7) and is locally overlapped by

imbricated boulder-sized bedrock clasts, which are torn up during storm events.

Sand flats are grain-dominated storm deposits at or just above MWL, some of which are

Table 2. Radiocarbon ages of shell fragments in little Ambergis Cay bedrock and interior basin sediment core samples.

Sample description	UCIAMS no.	Fig. 2 ID no.	Sample name	Fraction modern	±	$\Delta^{14}\text{C}$	±	^{14}C age (yr BP)	±
Cores and core top	218527	a1	VC03-030C shell frags	0.8811	0.0017	-118.9	1.7	1015	20
Cores and core top	218528	a1	VC03-070 shell frags	0.8598	0.0016	-140.2	1.6	1215	20
Cores and core top	218529	a1	VC03-180 shell frags	0.7303	0.0015	-269.7	1.5	2525	20
Bedrock (<i>Strombus</i>)	218532	a2	8/8 LI-1A shell	0.8998	0.0017	-100.2	1.7	850	15
Bedrock (<i>Strombus</i>)	218533	a2	8/8 LI-1B shell	0.9388	0.0020	-61.2	2.0	505	20
Bedrock (<i>Strombus</i>)	218534	a3	8/9 BB-5B shell.1	0.8593	0.0018	-140.7	1.8	1220	20
Bedrock (<i>Strombus</i>)	218535	a3	8/9 BB-5B shell 2	0.8643	0.0019	-135.7	1.9	1170	20
Bedrock (<i>Strombus</i>)	218536	a4	8/9 BB01-A shell	0.8636	0.0016	-136.4	1.6	1180	20

Table 3. Catalogue of microbial signatures in carbonate sediments observed on Little Ambergis Cay.

Type of microbial signature	Resultant structure	Representative figure(s)
A. Microbial growth on substrate		
1. Microbial mat	1. Flat, laminar, EPS-covered microbial mat overtopping ooids	1. 19A
2. Incipient growth	2. Cohesive ooids with pigmented organic-rich layers	2. 19B, 19C, 19D
B. Trapping and binding		
1. Sedimentation	1. Mat layer-bound irregular carbonate grains	1. 16C
C. Mechanical stress acting on biostabilized surfaces		
1. Erosion/scouring	1A. Erosional pockets of sand or hardground	1A. 14A, 14B
2. Gas pressure	1B. Mat roll-up structures	1B. 14J
3. Desiccation	1C. Angular mat intraclasts	1C. 14C
	1D. Rounded, inverted mat intraclasts	1D. 14D, 14E
	1E. Mat chips	1E. 14F
	2. Domes and folds/wrinkle structures	2. 14G, 14H, 14I
	3. Desiccation cracks	3. 14J
D. Biological response to physical disturbances		
1. Sedimentation	1A. Mat layer-bound irregular carbonate grains	1A. 16C
2. Desiccation	1B. Laminated levelling structures	1B. 16A, 16B
3. Influx of mat chips or intraclasts	1C. Mat-stabilized ripples	1C. 16D
	2A. Tufted, domed polygonal microbial mat with EPS-filled cracks	2A. 16E
	2B. Growth protruding outward over cracks	2B. 16E
	3. New growth in or on deposited mat chips or intraclasts	3. 14C; 16F, 16G, 16H
E. Post-burial processes and preservation		
1. Organic matter Decomposition	1. Faintly laminated pigmented grains	1. 19C
F. Grazing		
1. Grazing	1. Cerithioid gastropod shells	1. 14H

reworked by tides into channels with bars, with common centimetre-scale subaqueous wave oscillation, lags of cerithid gastropods, moulds

of mangrove stems and roots, and seagrass patches. Most channels in the island interior are lined with disaggregated organic material, large

(ca 4 to 12 cm) mat rip-up clasts, longitudinal bars, and wave-modified transverse bedforms reaching depths up to -1.5 m MWL. Much of the interior basin is floored with patchy, centimetre-thick ooid hardgrounds, *Batophora* algae and disaggregated organic material, typically either exposed over large areas or concentrated in metre-scale scour pits surrounded by smooth or polygonal mats. Mangrove-dominated regions of the north side of the cay contain luxuriant polygonal mats of variable thickness with sparse halophytes including sawgrass and *Salicornia*. Mangroves have an average DGPS elevation of -0.02 m MWL, comparable to that of smooth and polygonal mats. The DEM-based mangrove elevation is skewed by vegetation and should be disregarded.

Microbial mats are widespread in the island's interior, covering an area of more than 2.3 km², over a third of the island. Because populations of *Schizothrix* and *Scytonema* are indistinguishable between the mat morphotypes on Little Ambergris Cay (Trembath-Reichert *et al.*, 2016), mats are here distinguished based on their morphological expression. Microbial mats were grouped by texture and morphology into three categories: smooth mats, polygonal mats and blister mats. Such classification is important because it is these textural attributes that are imprinted in the rock record of carbonate textures (Demicco & Hardie, 1994). Smooth and polygonal mats are synonymous with the terms 'flat mat' and 'biscuit mat' (Trembath-Reichert *et al.*, 2016), or '*Schizothrix* mat' and '*Scytonema* mat' (e.g. Neumann *et al.*, 1970; Ginsburg & Hardie, 1975). The authors favour the term 'polygonal mat' over 'biscuit mat' as not all mats separated by polygon-forming cracks exhibit a convex surface. Blister mats are so named due to their fractured, colloform surfaces.

All mat morphotypes follow a subsurface vertical progression of millimetre-scale pigmented zonation typical of coastal microbial mat communities, stratified due to gradients in sunlight availability, oxygen and biogeochemical products (Van Gemerden, 1993; Soltz, 2000). The pigmentation progresses with depth from dark green or beige surface layers to lighter green, then purple and/or pink layers. Mat layers are sometimes intercalated with millimetre-thick laminae of carbonate sediment. Mat surfaces and/or depressions surrounding them are often covered with extracellular polymeric substances (EPS). Below the pigmented mat layers are up to several centimetres of degraded microbial mat organic matter containing remnant cyanobacterial sheaths. The mats are

underlain by ooid hardgrounds, ooids, minor-to-trace carbonate mud and minor skeletal sand.

The Ambergris mats are a complex ecosystem that hosts a diverse community of microorganisms that include cyanobacteria, most notably Alphaproteobacteria of the Rhodospirillales, Rhodobacterales and Rhizobiales; Chloroflexi of the Chloroflexales and Anaerolineales; Gammaproteobacteria of the Chromatiales; Deltaproteobacteria of the Myxococcales, Desulfovibrionales, Desulfobacterales and Syntrophobacterales; Planctomycetes of the Planctomycetales and Phycisphaerales; and Bacteroidetes of the Sphingobacterales (Trembath-Reichert *et al.*, 2016; Gomes *et al.*, 2020; Lingappa *et al.*, 2022).

Smooth mats form laterally extensive sheets that overlie ooids and ooid hardgrounds and are typically submerged under water. They are mostly developed in the open interior basin and its margins and exhibit several variants (Fig. 8). Polygonal mats are typified by deeply penetrating cracks with polygonal geometry; they occur commonly in the open interior basin and mangrove thickets and are intermittently submerged under water (Fig. 9). Blister mats have dark, cohesive, and usually rough or colloform surfaces and are rarely submerged under water, although they are often wet due to capillary rise of shallow groundwater (Fig. 10).

Water depth and exposure time of microbial Mats

Primary physical environmental factors that may influence the morphology of microbial mats on Little Ambergris Cay include hydrodynamic energy, subaerial mat exposure and sediment flux.

Water depth modelled from tide gauge data and the photogrammetric DEM provides a proxy for exposure time. The mean and standard deviation of DEM-based elevations of smooth, polygonal and blister mats are -0.14 ± 0.22 m, -0.01 ± 0.16 m and 0.06 ± 0.28 m MWL, respectively (Fig. 7, Table 1). The corresponding range of elevation distributions is unrealistically large, mostly due to the low vertical precision of the DEM (27.6 cm). The low vertical precision leads to a broad distribution of modelled elevations, but these errors are in most cases random, and thus the mean elevations should approximate the true average. This is supported by the similarity of mean elevations relative to DGPS data (Fig. 7). The elevations of sediment types measured with DGPS more accurately represent the true elevation range but are averaged over only tens to



Fig. 8. Plan view left, cross-section right. Surface and cross-sectional images of mats of the ‘flat mat’ morphotype. (A) Smooth, often extracellular polymeric substances (EPS)-covered (sometimes dark green), highly cohesive, 3 to 5 cm thick mats with incipient low-lying cracks forming incomplete polygons; (B) cross-section of (A); (C) smooth, centimetre to decimetre-thick, EPS-covered, low-cohesion mats; and (D) cross-section of (C).

hundreds of measurements, making the mean more susceptible to outliers. The DGPS elevations of smooth, polygonal and blister mats $\pm 1\sigma$ are -0.02 ± 0.03 m, 0.00 ± 0.04 m and 0.08 ± 0.24 m MWL, respectively (Fig. 7, Table 1).

Collectively, the best estimate of mean sediment type elevation and elevation range results from combining the DEM-based means and DGPS-based ranges, which reconciles the strengths and weaknesses of each method. Smooth mats occur on average *ca* 14 cm below MWL and 1 to 2 cm below the mean low tide measured during July 2018. Ninety-five percent of smooth mat elevations are between -0.20 to -0.08 m MWL, which closely mirrors *in situ* observations and corresponds to a modelled average daily exposure time of 0 to 12 h and an average water depth up to *ca* 0.5 m at high tide for the lowest mats. The average smooth mat elevation was always underwater during our measurements. Polygonal mats occur on average *ca* 1 cm below MWL with 21 h of average daily exposure. Ninety-five percent of polygonal mats are between

-0.08 to 0.02 m with *ca* 12 to 23 h of average daily exposure, consistent with our observations that polygonal mats were subaerially exposed for more than half of our survey periods. The average elevation of blister mats is *ca* 0.06 m above MWL, which is on average exposed 24 h per day. Ninety-five percent of blister mats are between 0.01 m and 0.30 m, which ranges in daily exposure time from 22 to 24 h. The elevation distribution of blister mats is broader than the other mat types, consistent with observations that blister mats were found at high elevations abutting bedrock or in inactive or abandoned channels (for example, Fig. 11). Despite being so exposed, even the highest elevation blister mats are moistened by capillary ground water rise. Additionally, because these measurements were based on tide data gathered over a six-day period in July 2018, it is possible that higher tides during other seasons may lead to slightly less exposure of high-lying mats during those times. Few mats were identified below -0.2 m MWL, which is close to the average elevation of the ooid hardground

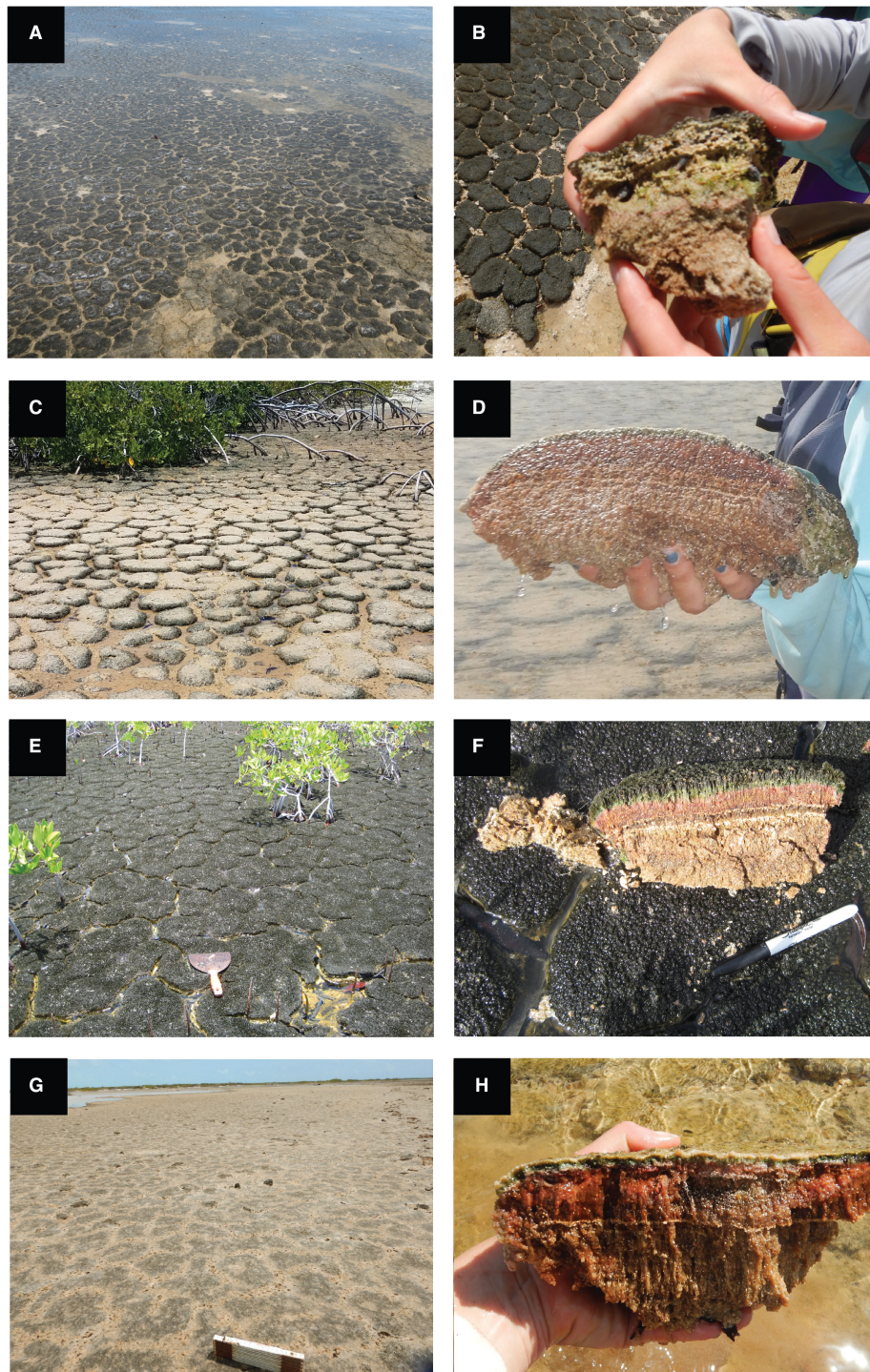


Fig. 9. Plan view left, cross-section right. Surface and cross-sectional images of mats of the 'polygonal mat' morphotype. (A) Highly cohesive, domed, centimetre-thick, somewhat dry, dark green and sometimes tufted surfaces and extracellular polymeric substance (EPS)-filled cracks forming 5 to 15 cm wide polygons in the island's interior basin; (B) cross-section of (A); (C) highly cohesive, domed, centimetre-thick, somewhat dry with dark green and sometimes EPS-covered surfaces and large, recessed cracks forming 5 to 15 cm wide polygons; (D) cross-section of (C); (E) slightly domed, decimetre-thick, highly cohesive mats with dark green tufted surfaces and recessed EPS-filled cracks forming 10 to 20 cm wide polygons, commonly near mangroves; (F) cross-section of (E); (G) flat, decimetre-thick, low-cohesion EPS-covered mats with EPS-filled cracks forming 5 to 15 cm wide polygons in the island's open interior; and (H) cross-section of (G).

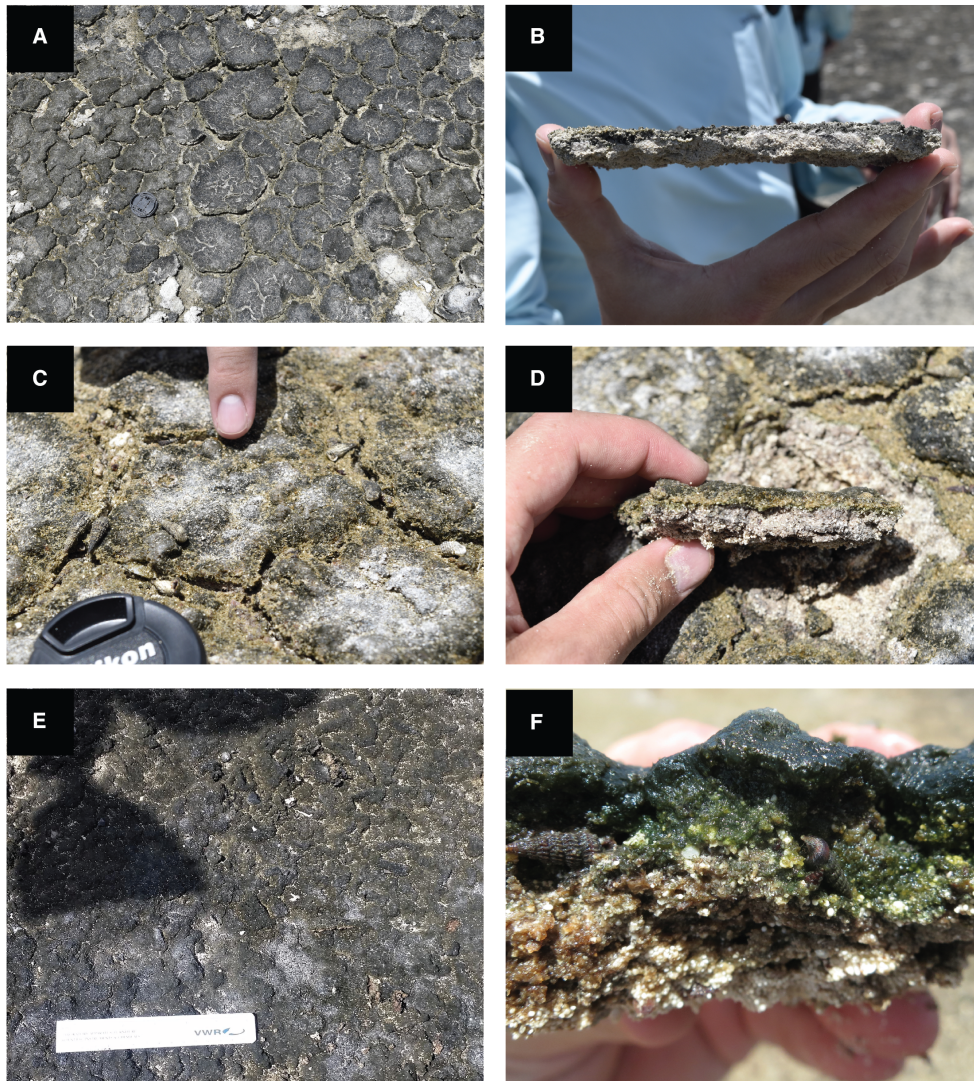


Fig. 10. Plan view left, cross-section right. Surface and cross-sectional images of mats of the ‘blister mat’ morphotype. (A) Dry, leathery, cracked, often botryoidal, halite-covered, millimetre-thick material with upturned margins overlying ooids and often interspersed with mat chips; (B) cross-section of (A); (C) mostly flat, centimetre-thick, dry mats with dark green surfaces sometimes covered in halite, with cracks that form 5 to 10 cm thick polygons; (D) cross-section of (C); (E) leathery, black, often botryoidal, centimetre-thick surface overlying ooids and sometimes covered in halite, sometimes with tufted surfaces, domes from outgassing and mat chips; and (F) cross-section of (E).

floors in the interior basin on which mats accumulate. The mean elevation of the ooid hard-ground sediment type in DGPS data is -0.12 m, putting it *ca* 5 cm below the mean low tide level and 10 cm below the mean DGPS smooth mat elevation. The mean elevation of the ooid hard-ground sediment type in DEM data is -0.152 m, *ca* 8 cm below the mean low tide level and *ca* 1 cm below the mean DEM smooth mat elevation.

Hyperspectral imaging also reveals a link between elevation and the abundance of

photosynthetic pigments. The surfaces of smooth mats have deeper chlorophyll *a* absorption band depths, which can be related to chlorophyll *a* abundance (Figs 5G and 12A), a proxy for high gross primary productivity (e.g. Gitelson *et al.*, 2006). The high band depth could instead result from the presence of darkening agents. Although the spectrometer did not overlap with the wavelength of ultraviolet-screening compounds like scytonemin (Proteau *et al.*, 1993; Fleming & Castenholz, 2007), mat surfaces were observed to

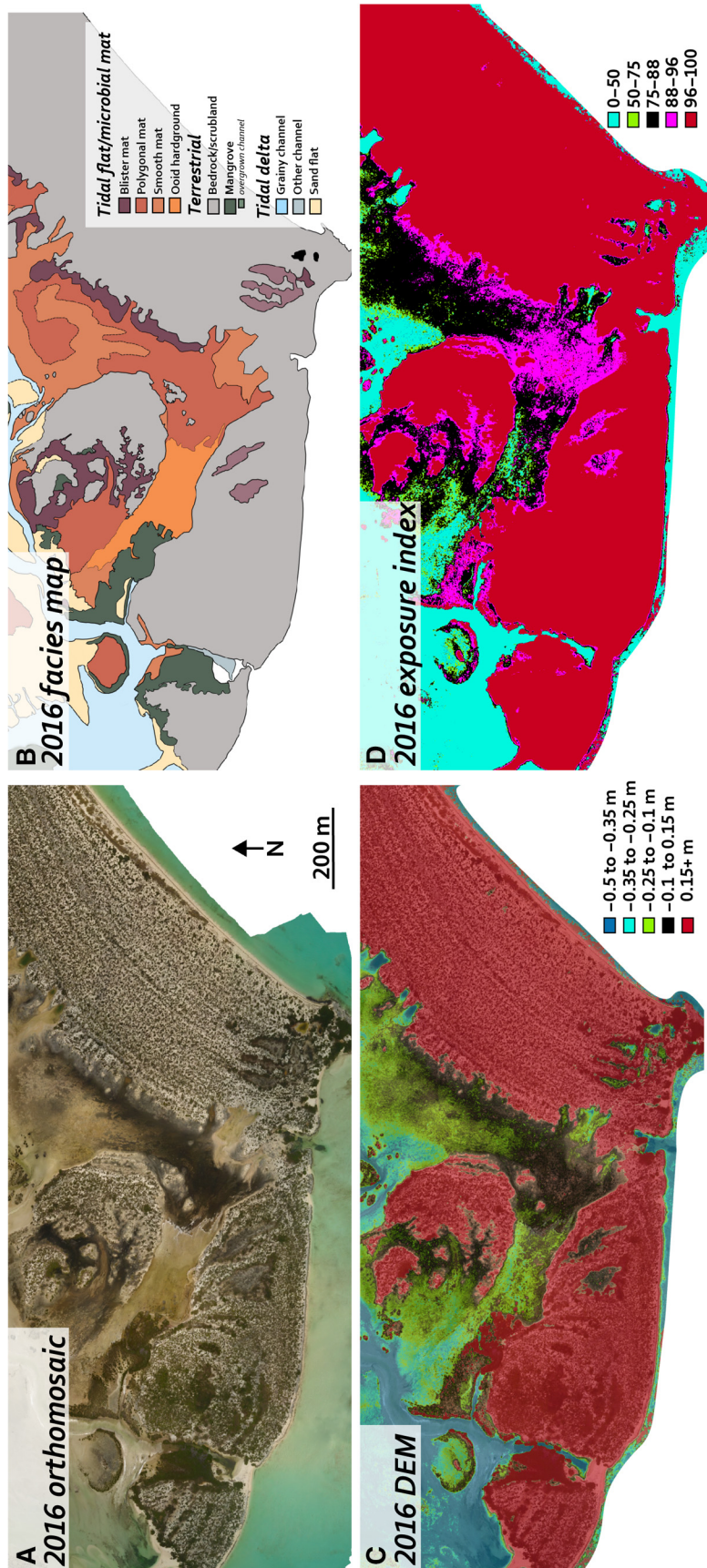


Fig. 11. Spatial distribution of mat morphotypes on the southern portion of Little Ambergris Cay showing a wide distribution of average exposure time over short distances. (A) Subset of the 2016 Little Ambergris Cay RGB uncrewed aerial vehicle (UAV) orthomosaic showing a region with the three mat morphotypes. (B) Sediment type map of the same region. (C) UAV-based elevation model binned by elevation and overlaid on the RGB orthomosaic. (D) Modelled exposure index of the same region.

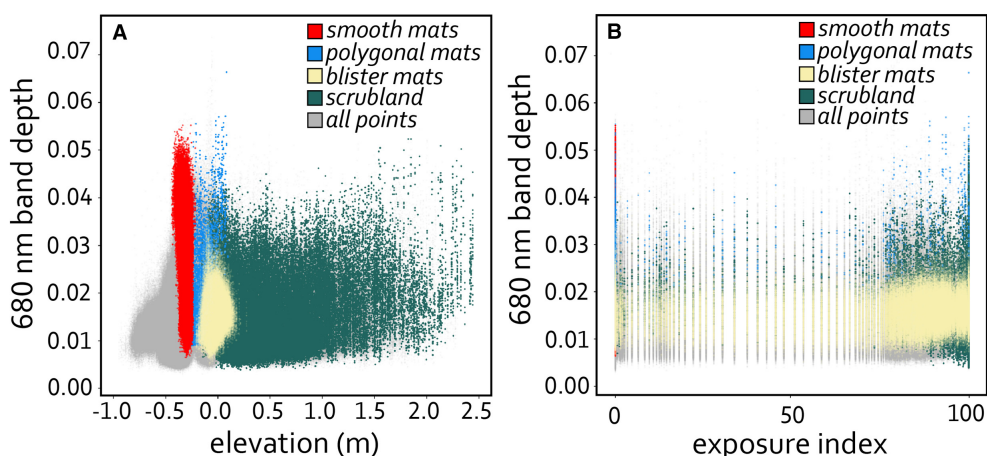


Fig. 12. (A) 680 nm band depth (Chl. *a* abundance) as a function of elevation extracted from the representative scene in Fig. 3A. Smooth mats, polygonal mats, blister mats and scrubland are colour coded. Scrubland includes a mixture of shrubs and bedrock. (B) 680 nm band depth as a function of exposure index from the same scene.

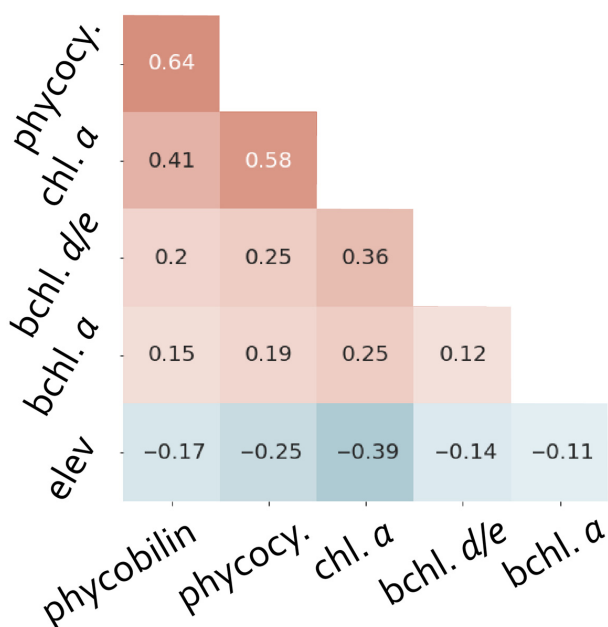


Fig. 13. Correlation coefficient between the major pigment abundance and elevation measured from the representative scene in Fig. 5.

darken with increasing elevation, evidenced by a consistent decrease in reflectance between flat, polygonal and blister mats. Polygonal and blister mats have a consistently shallower 680 nm absorption feature (Figs 5B, 5G and 12A). Chlorophyll *a* band depth is negatively correlated (*ca* -0.6) with elevation (Figs 12A and 13), suggesting higher productivity with decreasing exposure. Figure 12B

shows that the highest chlorophyll *a* abundance corresponds to subtidal smooth mats and continuously exposed terrestrial vegetation. Smooth mats also have a higher abundance of phycobilin, phycocyanin, and bacteriochlorophylls *a*, *d* and *e* (Fig. 5E, F, H and I) relative to polygonal mats, which in turn have a higher abundance of these pigments than blister mats. The abundance of these pigments also has a weak to moderate negative correlation with elevation (Fig. 13).

Impact of physical stresses on mat texture

Major physical stresses that modify biostabilized surfaces on Little Ambergris Cay include: (i) gas pressure; (ii) desiccation; and (iii) erosion/scouring (Fig. 14).

The production and diffusion of microbially-generated gas provides pressure against the cohesive surface from below, deforming the surface upward. Resulting structures identified in the field include 3 to 10 cm diameter, 1 to 5 cm tall domes with a hollow centre that were susceptible to collapse (Fig. 14G), as well as elongated, 1 to 5 cm tall folds of new mat material (Fig. 14H and I).

Measurements of >1500 mat polygons (for example, Fig. 15) show desiccation cracks that meet at an average vertex angle of 120° , forming 50 to 350 cm² polygons. The cracks range in width from *ca* 0.5 to 2.0 cm and penetrate as far as the underlying substrate. 120° vertex angles are consistent with multiple wetting and drying cycles, which modify cracks that originally meet



Fig. 14. Microbial morphologies arising from physical stress acting on biostabilized surfaces (Table 3C). (A) Aerial view of scoured pockets of microbial mat in the island interior following Hurricane Irma in September 2017. (B) Incised, mat-stabilized channel formed during Hurricane Irma in September 2017. (C) Angular, centimetre-scale microbial mat intraclasts mixed with ooids, carbonate mud and organic debris. (D) Rounded microbial mat intraclasts formed by the erosion of polygonal microbial mat in strong currents. (E) Close-up view of a single rounded microbial mat intraclast, which is typically deposited with the most recent surface layer on the bottom, as shown, due to its relatively high density. (F) Mat chips embedded in ooids and bound in a matrix of subsequent microbial growth. (G) Collapsed gas dome. (H) A mat fold from gas pressure. (I) Area with ubiquitous mat folds. (J) Desiccated mat with upturned edges that break off as roll-up structures. The trowel in (D) is 10 cm across at its widest point. The folded ruler in (F) and (G) is 20 cm long. The tool in (H) is 15 cm wide at its base. The lens cover in (J) is 52 mm across.

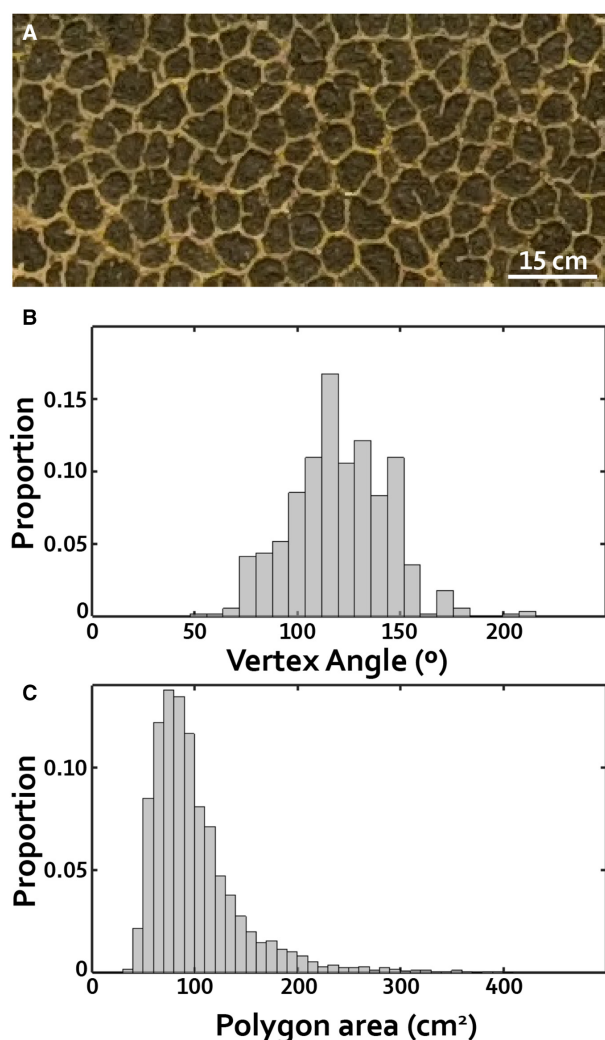


Fig. 15. (A) Subset of uncrewed aerial vehicle (UAV)-based RGB image of polygonal mats on Little Ambergris Cay. (B) Vertex angles formed by >1500 junctions of the cracks that create polygons. (C) Distribution of the area of polygons.

at 90° angles (Goehring *et al.*, 2010). Subaerial exposure and rewetting of microbial mats occurs tidally, with mats being submerged for several

hours during high tide and exposed for the rest of the day (*Water depth and exposure time of microbial mats* section). The polygons are often domed in response to differential drying, producing a characteristic ‘biscuit’ morphology (Figs 9 and 16E). Highly desiccated mats exhibit raised edges that may break off as roll-up structures (Fig. 14J). Not all blister mats are cracked, likely because they are thin and lack the cohesion necessary for cracks to develop.

Erosion and scouring of microbial mats occur most commonly during storms when hydrodynamic forces overwhelm cohesive forces within the mats or between the mats and underlying substrate. In the interior basin, erosion often results in steep-edged gullies in the microbial mat surface up to several metres wide and 2 to 15 cm deep (Fig. 14A). The erosional pockets coalesce in some areas, creating irregularly shaped patches of polygonal microbial mats that rise above the oolitic substrate; their margins are aligned with the preferential current flow during large storm events. Most storm-related erosional work on mats occurs in the interior basin. However, tidal channels cut back into tidal flats with microbial mats during major storms, indicating that mats do not prevent erosion during strong flows (Fig. 14B).

Mat intraclasts (Fig. 14C and D) are thin, angular-to-rounded fragments of organic material that break free from mat stabilized ripples, domes, folds or roll-up structures. They form when hydrodynamic forces undercut mats, but individual textural elements that comprise the mat fragment (clast) remain intact. Mat intraclasts form by breaking from polygonal mats during strong storms and are rounded during transport into ellipsoidal, highly cohesive, 10 to 20 cm wide clasts that are redeposited in the interior basin (Fig. 14D and E). They are typically deposited upside-down, with the surficial layers on bottom and lower layers on top, due to their density profile. Thousands of mat



Fig. 16. Examples of microbial structures arising from a biological response to physical stresses (Table 3D). (A) A level surface created by microbial growth on sediment deposited on polygonal mats. (B) Cross-sectional view of (A) showing mature polygonal microbial mats separated and overtopped by sediment and covered in new microbial growth. (C) Layers of bound irregular carbonate grains in a mature microbial mat. The yellow arrows denote four separate layers of bound grains, with the uppermost being deposited during Hurricane Irma in September 2017. Each black line is 1 mm. (D) Sand ripples with *ca* 10 cm wavelength and rounded crests stabilized by subsequent microbial growth. (E) Mature polygonal mats. (F) A green cyanobacteria and overlying tan extracellular polymeric substance (EPS) layer growing in filaments of a rounded and overturned mat intraclast (see Fig. 14D and E). (G) Mature polygonal microbial mat overgrowing a rounded, overturned mat intraclast from the north-west side of the island. The boundary between the intraclast and new growth is denoted by the upper arrow. The lower arrow shows the overturned cyanobacteria layer of the intraclast, which still exhibits tufts. (H) Another example of mature polygonal microbial mat overgrowing a rounded mat intraclast (boundaries denoted by yellow arrows).

intraclasts were observed throughout the island interior following Hurricane Irma in erosional depressions in the interior basin, along ooid grainstone margins, in the roots of mangroves, and as lag deposits abutting overwash fans. Angular mat intraclasts observed after the storm (Fig. 14C) likely have similar provenance but experienced less rounding during transport.

Subsequent microbial growth may occur in or on mat intraclasts deposited in the intertidal zone. In March 2018, six months after Hurricane Irma, green pigments indicative of cyanobacterial growth and a millimetre-thick EPS layer had developed within the fabric of overturned rounded mat intraclasts (Fig. 16F). Rounded, overturned mat intraclasts from previous storms, such as those observed after Hurricane Kate in 1985 on North Caicos (Wanless *et al.*, 1988), are preserved below several centimetres of thick polygonal mats (Fig. 16G and H), indicating that the production, burial and overgrowth of mat intraclasts has occurred repeatedly on Little Ambergris Cay.

Radiocarbon dating, subsurface sedimentology and mat preservation

The ^{14}C ages of *Strombus* shells collected from the most seaward exposures of the Holocene cemented beach ridges range from 480 ± 20 to 1220 ± 20 radiocarbon years (Table 2). Samples were not collected from more inland or eastern portions of the beach ridge rim, which may be older. ^{14}C ages of cerithid gastropods from sediment cores collected in the interior basin range from 850 ± 20 to 2525 ± 20 radiocarbon years (Table 2).

The depth to lithified bedrock ranges within the interior basin from >250 cm to less than 20 cm below the surface with a median of 70 cm (Fig. 4B). Three representative cores collected at sites with each mat type are shown in Fig. 17 (see Present *et al.*, 2021, for remaining cores). Beneath the most recent microbial mat layer, the subjacent sediment was composed of fossiliferous ooid sands, mostly unlithified, except for sparse, small concretions. The ooid sands show textural evidence of dissolution (Present *et al.*, 2021). Skeletal grains included gastropods (predominantly high-spired), coralline algae, bivalves, serpulid worm tubes, foraminifera, minor arthropod and fish fragments, and *Halimeda*, generally consistent with an upper shoreface or high-energy

shoal assemblage (Present *et al.*, 2021). Angular intraclasts of reworked hardgrounds, cerithid gastropods and minor muddy intervals consistent with a restricted, evaporative environment, were also observed throughout most cores, indicating that much of the core deposition may have occurred in a restricted environment regularly perturbed by high-energy events (Present *et al.*, 2021). Only traces of intercalated microbial mats were preserved; one core (VC-05, pre-Irma, Fig. 17) that was buried under several centimetres of sediment during Hurricanes Irma (2017) and Ike (2008) contains a faintly laminated, *ca* 1 cm thick pigmented horizon 60 cm below the surface (Fig. 18A), likely from before either storm. The VNIR spectrum of the organic material (Fig. 18B) contains absorption features at *ca* 680 nm and between 775 to 900 nm consistent with chlorophyll *a* and bacteriochlorophyll *a*, respectively (Hubas *et al.*, 2011).

DISCUSSION

Controls on microbial mat extent and texture

Two observations indicate that hydrodynamic forces and subaerial exposure are the primary factors that determine the texture and distribution of microbial mats on Little Ambergris Cay: (i) the three mat morphotypes occupy distinctive elevation ranges that correspond to different water depths and subaerial exposure time (Figs 3 and 7); and (ii) surface textures consistent with desiccation or organic decomposition are observed in conjunction with increasing exposure time (Fig. 14).

Based on our collective measurements, smooth mats are found only in the subtidal and lower intertidal zones and experience limited subaerial exposure. Few smooth mats are found below -0.2 m MWL (*ca* 0.55 m below mean high tide), likely because relatively high hydrodynamic forces prohibit attachment to the underlying substrate. As a result, much of the western interior basin is floored by extensive ooid hardgrounds. Polygonal mats are more desiccated, on average 14 cm higher in elevation than smooth mats and inhabit portions of the lower and upper intertidal zones, especially in mangrove-dominated areas. Polygonal mats are exposed subaerially for 10 to 23 h each day, compared to 0 to 12 h for smooth mats. Such a drastic change, which is responsible for the formation of domed polygons, is a consequence of the sensitivity of exposure time to

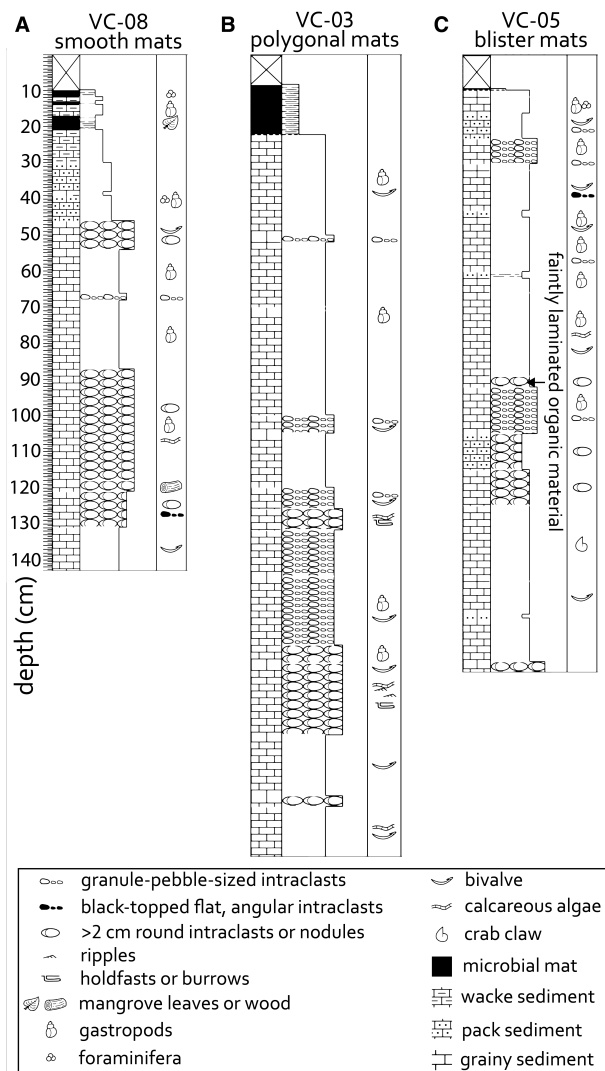


Fig. 17. (A) VC-01 sediment core of area covered by polygonal mats with no preserved mat material below the surface. (B) VC-03 sediment core of area covered by smooth mats with no preserved mat material below the surface. Samples listed in Table 2 were taken from this core at depths of 30 cm (VC03-030C), 70 cm (VC03-070) and 180 cm (VC03-180). (C) VC-05 sediment core of area covered by blister mats with putative preserved mat material *ca* 60 cm below the surface. Core locations are shown in Fig. 2.

water depth; daily exposure time differs by as much as 15 h over elevation differences of less than 5 cm (Fig. 3D). Blister mats are more desiccated still, exposed for 22 to 24 h per day and colonizing up to 30 cm above MWL where they exhibit surface textures resulting directly from desiccation (cracks, convex-up margins and evaporites) and organic decomposition (gas domes and folds). Reflectance spectra show that the

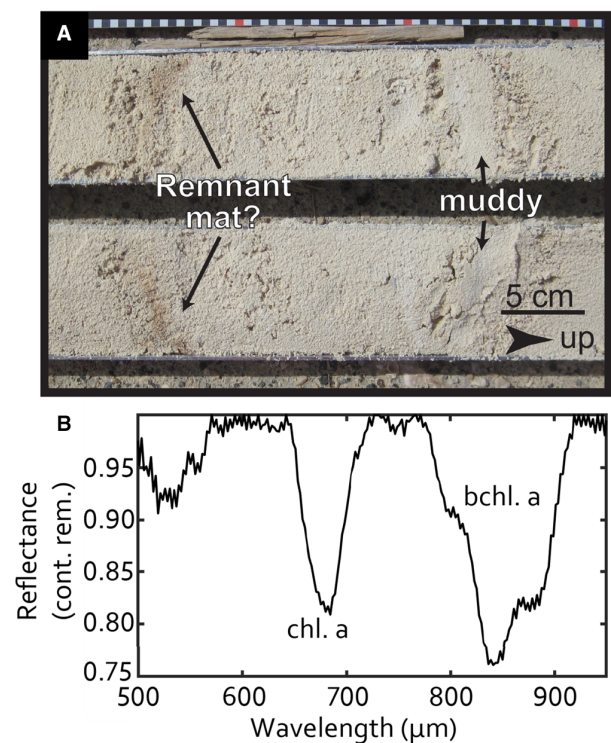


Fig. 18. (A) Cross-section of the only core with potential preservation of faintly laminated microbial mat material down core, *ca* 60 cm below the surface (VC-05C). (B) Continuum removed reflectance spectrum of the putative preserved organic material in (A) showing characteristic absorption features of chlorophyll *a* and bacteriochlorophyll *a*.

smooth mats exhibit generally deeper Chl. *a* and Bchl. *a*, *d* and *e* absorption features than the more exposed mats, consistent with higher productivity that diminishes with desiccation and/or reduced presence of dark, light-quenching pigments. The microbial community composition of the mat morphotypes shows surprising uniformity. While subtle differences distinguish the microbial communities between mat morphotypes, their overall community compositions are similar (Lingappa *et al.*, 2022). Hence, the wide diversity of textures and sedimentary structures observed in mats on Little Ambergris Cay is primarily attributable to desiccation resulting from small elevation differences, not to microbial community composition or ecological succession.

Exposure time alone cannot account for the full range of microbial structures observed on the island; powerful storms play a critical role in the mechanical erosion and the distribution of mats resulting from sediment delivery to the interior basin. In parts of the basin, thick (often

recurring) storm deposits completely smother underlying mats (Jamison-Todd *et al.*, 2020; Present *et al.*, 2021). Elsewhere, thinner sediment deposits either dissipate before the underlying mats are smothered, are recolonized by entrained and resettled organisms, or are traversed and recolonized by underlying motile microorganisms, leading to the trapping of mat layer-bound irregular carbonate grains. Erosion during the strongest storms rips up broad tracts of mats – up to hundreds of m² per event – in the open interior basin and redeposits them as mat intraclasts. In cross-section, the most spectacular mats display mat intraclasts from previous storms overgrown by multiple centimetres of cyanobacterial sheaths and several horizons of carbonate grain storm lags preserved within the layered mat biomass.

Recovery of microbial mats following sediment-blanketing storms

Although mat surface texture is dominated by long-term response to subaerial exposure, storm events help control on microbial fabrics because they modify biostabilized surfaces and influence the spatial distribution of microbial mats. Tropical storms and hurricanes produce strong hydrodynamic forces (*Impact of physical stresses on mat texture* section) and spread sediment throughout the interior basin, both as a thin veneer of ooid sand (transported in suspension in the storm surge) and as thicker, locally emplaced layers of sediment such as washover fans (Wanless *et al.*, 1988; Jamison-Todd *et al.*, 2020; Present *et al.*, 2021). The distribution and thickness of storm-deposited sediment, as well as how long it smothers underlying mats, significantly influences the recovery of microbial mats. Our observations suggest that mats can be smothered by a critically thick layer of sediment. Below this thickness filamentous cyanobacteria may migrate upward between ooid grains and spread laterally, trapping the underlying grains in place (Grotzinger & Knoll, 1999; Trower *et al.*, 2019). Above this critical thickness, subsequent mat growth may require recolonization (for example, Fig. 19) and/or the surface remains above water. This critical thickness was observed to be 2 cm on Little Ambergris, although Wanless *et al.* (1989) observed the smothering of some mats with only a millimetre-thick storm layer following Hurricane Kate.

The predominant textural evidence of biological responses to sedimentation includes trapped and bound carbonate grains, laminated levelling

structures (laminated mat fabrics infilling depressions) and mat-stabilized ripples. Grains are trapped and bound when microbes respond to an influx of sediment by migrating upward towards the new surface and spreading laterally, stabilizing thin layers of sediment below and leaving alternating layers of sediment and microbial sheaths that represent former mat surfaces (for example, Fig. 16C). The recolonization process may repeat during subsequent sedimentation events, leaving sediment and sheath couplets with biomass layers of variable thickness depending on the duration of the quiescent period. Hurricane Irma deposited a *ca* 1 to 2 cm thick layer of ooids and carbonate grains over much of the interior with localized deposits >50 cm thick (Jamison-Todd *et al.*, 2020). Tidal currents likely removed this layer from most of the interior basin by March 2018 except in mangrove-dominated areas with higher tidal friction. Cross-sections of the polygonal mats from these areas reveal at least 3 mm thick lags of irregular carbonate grains separated by varying thicknesses of remnant biomass (Fig. 16C). The uppermost grain layer, deposited during Hurricane Irma, was overgrown by a millimetre-thick layer of new cyanobacterial tufts by March 2018 (Fig. 16C) (Lingappa *et al.*, 2022).

When sediment fills and levels depressions between polygonal microbial mats, subsequent microbial growth results in a level mat surface (Fig. 16A), which is expressed in cross-section as laterally distinct sets of laminated mat fabric and disaggregated sand (Fig. 16B). This dynamic supports numerical models of stromatolite morphogenesis that explore surface roughening and surface smoothing by mat growth and competing sedimentation (Grotzinger & Knoll, 1999). When low enough to remain wet, sand ripples formed in the lower supratidal zone at the end of storm events are sometimes colonized at the surface and stabilized by cyanobacteria (Fig. 16D). Once stabilized, the ripples can withstand moderate shear from water during storms and high tides (Neumann *et al.*, 1970; Scoffin, 1970; Mariotti *et al.*, 2014). Organisms may colonize and stabilize the lower ripple troughs, allowing preferential erosion of the ripple crests to produce flat-topped ripples. Erosion of biostabilized ripples produces mat chips deposited down-current from ripples.

Development of microbial mats on Little Ambergris Cay: A synthesis

The growth of thick microbial mats on Little Ambergris Cay within the context of a



Fig. 19. Microbial growth on substrate (Table 3A). (A) Stereotypical, well-developed smooth mat overlying ooids. (B) Incipient, sub-millimetre-thick, pink-toned organic material and green-toned cyanobacteria overlying ooids and remnant mat material (yellow arrow) in the island interior. (C) Close-up view of (B). (D) Dark toned, sub-millimetre-thick cyanobacteria overlying ooids in the island interior: (D) is classified as blister mat.

surrounding high-energy platform was enabled by accretion of a beach ridge rim that created a sheltered and interior basin. Sediment accretion to form the beach ridges was (and still is) driven by persistent easterly trade winds, which control Holocene patterns of carbonate sedimentation across the Caicos Platform (Dravis & Wanless, 2017). Shallow subtidal ooid shoals on the Caicos Platform, including Ambergris Shoal, are oriented parallel to the easterly trade winds

(Rankey *et al.*, 2008; Dravis & Wanless, 2017; Trower *et al.*, 2018). Consistent wind–wave agitation maintains the transport of grains that feed Ambergris Shoal and drive ooid formation. Wave fronts impinge on Big Ambergris Cay, a >25 m tall Pleistocene island 2 km east of Little Ambergris Cay, approximately parallel to its eastern shoreline and are refracted, creating two wave sets that converge on the northern and southern shorelines of Little Ambergris Cay and then nearly obliquely

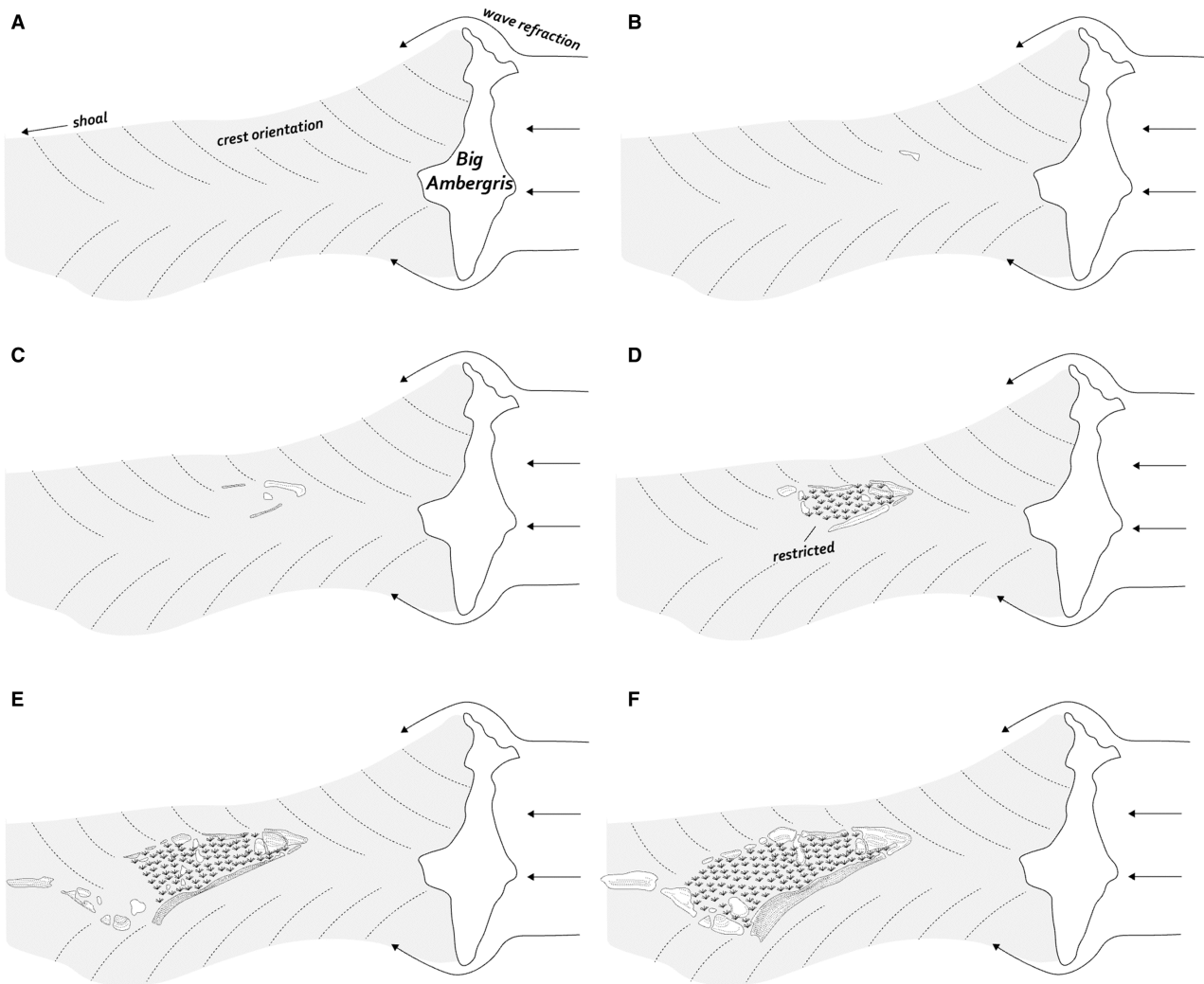


Fig. 20. Interpretive scenario for the initiation and evolution of Little Ambergris Cay as a tombolo. Big Ambergris is assumed to have a constant extent over the duration of Little Ambergris Cay's formation. (A) Waves driven by consistent easterlies refract around Big Ambergris and converge in the lee. (B) Sediment accumulates in the lee of Big Ambergris, initiating shoreface accretion of oolitic sand. (C) Wave baffling in the lee of initial bedrock ridges promotes further sedimentation to the west. (D) Oolitic beach ridges and dunes prograde outward orthogonal to the direction of wave convergence, partially enclosing a restricted region. (E) and (F) Progradation and westward growth continue until the island reaches its present form.

on the main shoal (Fig. 20A) (Wanless & Dravis, 2008; Trower *et al.*, 2018).

Oolitic grainstones that comprise the rim are interpreted to have formed in an upper shoreface to backshore depositional setting. Shoreface accretion of oolitic sand likely initiated in the lee of Big Ambergris Cay thanks to consistent delivery of sediment by converging wave fronts, akin to tombolo or salient formation (both sand spits forming in the lee of an obstacle) (Fig. 20A and B). Continuous accretion of the beach ridge rim began recently. The presence of cerithid gastropods downcore

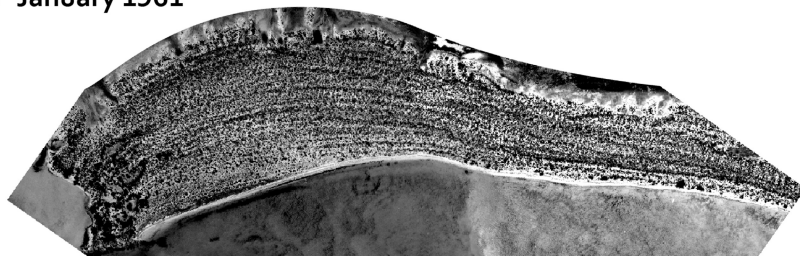
(Present *et al.*, 2021), which burrow into and may graze on mats, indicates that portions of the interior basin may have been restricted for millennia. One potential island formation scenario is that wave baffling in the lee of initial beach ridges promoted *in situ* growth of oolitic sand and rapid sedimentation and growth of south-west and north-west-trending beach ridge complexes that extended the island westward, eventually partially enclosing a peritidal interior basin (Fig. 20B to E). Dravis & Wanless (2017) proposed a similar scenario for the evolution of upper Pleistocene and

Holocene oolitic beach ridges of West Caicos, which likely formed due to ooid sand refraction around Pleistocene ridges and subsequent long-shore transport. Another possible scenario is that Little Ambergris Cay formed from the maturation of a double tombolo/salient (e.g. Owens, 1982) that enclosed a restricted region. Sedimentation in the lee of manmade breakwaters is commonly focused within distances shorter than their length (e.g. Mangor *et al.*, 2017), as is the case with Little and Big Ambergris Cays. ^{14}C ages of lithified beach ridges on the western tip of Little Ambergris Cay as recent as 505 ± 20 (8/8 LI-1B shell) radiocarbon years (Table 2) support rapid westward expansion. Outward progradation of the oolitic beach rock and eventually subaerial aeolian dunes extended the beach ridge rim to the north and south (Fig. 20D to F). This progradational process may have been supported by one or more Holocene sea-level stands. Critically, this type of progradation is ongoing; comparison of recent drone orthomosaics with aerial survey photographs from February 1961 shows tens of metres of seaward progradation on the south side of the island over the last 60 years (Fig. 21).

The observed sensitivity of mats to elevation could indicate that they are a recent phenomenon on Little Ambergris Cay, arising only after sediment infill raised the interior elevation. However, ample evidence of cerithid gastropods, angular crust intraclasts and mangrove debris unique to an interior basin suggest that a similar type of restricted environment has been present for hundreds of years (Present *et al.*, 2021).

Specifically, cerithid gastropods are observed in cores at depths of 10 to 200 cm (Fig. 17) with ages of 505 ± 20 to 1220 ± 20 radiocarbon years (Table 2). The interpretation that microbial mats have been present on Little Ambergris since the formation of the interior basin faces some challenges. First, little organic material is preserved in cored sediment. Rapid decay of buried mats was also evident months after Hurricane Irma (for example, Fig. 18A). Present *et al.* (2021) propose that the microbial mats are not currently preserved because aerobic respiration and sulphide oxidation result in porewaters with low aragonite saturation indices (<2.5), the lowest of which inhibits lithification. In this scenario, rapid respiration driven by highly productive microbial ecosystems may decrease their preservation potential. Second, although mats exist within a limited elevation range (*ca* -0.2 to 0.3 m MWL), the depth to basement rock exceeds 2 m across much of the interior (Fig. 4B). For mats to have persisted in a restricted environment, sediment accumulation would have to be balanced by accommodation creation by some combination of eustasy, subsidence, dissolution, compaction and sediment transport. Holocene sea-level change is well-documented in the Caribbean (e.g. Fleming *et al.*, 1998; Toscano & Macintyre, 2003; Milne *et al.*, 2005). Toscano & Macintyre (2003) inferred an average sea-level rise of $0.93 \text{ mm year}^{-1}$ for 2000 years before present, which would yield a *ca* 2.0 to 2.5 m sea-level increase since the oldest sediment core ^{14}C ages. Khan *et al.* (2017) arrived at a similar sea-level increase of 1.4 ± 0.5 m in the

A January 1961



B June 2016



Fig. 21. (A) British aerial survey photograph of bedrock on the south side of Little Ambergris Cay taken in February 1961. (B) The same location imaged by uncrewed aerial vehicle (UAV) in June 2016 with a trace of the shoreline from (A). Images were aligned by warping the survey photograph to the 2016 orthomosaic using manual tie points.

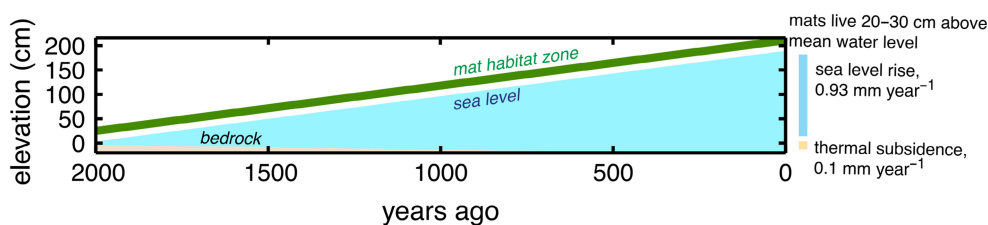


Fig. 22. Notional history of the absolute elevation of mat-inhabited zones in which sediment accumulation is balanced by sea-level rise and thermal subsidence, allowing mats to persist at the surface within a restricted elevation range.

Bahamas over the last 2000 years. Hence, mats could have grown over a long period in a restricted peritidal environment well below the modern absolute elevation of the interior basin (Fig. 22). Other processes could have acted to lower the surface elevation of the interior. Evidence of subsidence in the Caicos Platform is limited, but modest thermal subsidence of 0.1 mm year^{-1} (Maloo & Grotzinger, 2012) would have lowered the interior by 0.2 m over the same period. Additionally, carbonate grain dissolution observed in the sediment cores (Present *et al.*, 2021), compaction, and aeolian and tidal current sediment transport could plausibly cumulatively offset sedimentation to permit persistent, unpre-served mat growth for hundreds of years.

SYNTHESIS AND CONCLUSIONS

Modern environments with broad tracts of thick (>10 cm) microbial mats are relatively rare globally. Little Ambergris Cay hosts a rare example of luxuriant microbial mats growing in a restricted, low energy environment within an overall high energy platform setting. Mats in the interior basin of Little Ambergris Cay are protected from persistent converging wave fronts driven by strong easterly winds. Converging wave fronts deposited sediment in the lee of the adjacent Big Ambergris Cay to develop the restricted environment during the latest Holocene time. The precise events by which the restricted basin developed are unclear and require further study; perhaps outward progradation began nearly contemporaneously from many points or the elongated northern and southern shorelines developed akin to a double tombolo that quickly enclosed an interior region. Regardless, rapid cementation likely played a crucial role in stabilizing the bedrock rim against storm overprinting and permitting

further accretion. Some mats in the interior are further shielded by mangroves. The most luxuriant mats grow among mangrove roots, which protect them during storms that rip up broad tracts of mats from the interior. Indeed, carbonate grain lags from multiple storms are observed in mats throughout the mangroves, indicating that they have survived multiple hurricanes (including Category 5 Hurricane Irma).

Luxuriant microbial mats developed within high-energy settings are rare on modern platforms, uncommon in the stratigraphy of ancient Phanerozoic platforms, but more abundant within Precambrian platforms where transgressive flooding occurred (e.g. Grotzinger, 1989) in zones of sustained palaeotradewinds (Hoffman & Grotzinger, 1993). Although ubiquitous, it is possible that these microbial mats on Little Ambergris Cay will be poorly preserved due to the early diagenetic chemistry associated with their shallow burial; however, their former presence could be indirectly established through the presence of restricted fauna, coupled with the presence of biomarkers and organic residues indicative of former microbial mats (Present *et al.*, 2021). The detection of such features would indicate shoal development that advanced to the point of creating interior basin peritidal environments. Furthermore, our observations on Little Ambergris demonstrate that mat morphology, and therefore expected stromatolite morphology, reflects the physical environment, not microbial diversity. Finally, the factors that control mat morphology and sedimentological texture are sensitive to small changes in environmental conditions, and as a result the most widespread mats exist in a narrow niche where the physical environment provides sufficient subaerial coverage but does not erode the mats. This is important for the interpretation of mat textures in the rock record where subtle changes in sea level could result in significant changes in texture.

ACKNOWLEDGEMENTS

We thank the Agouon Institute for funding and the Turks and Caicos Islands Department of Environment and Coastal Resources for permitting this research. EJT and MLG were funded by NASA grant 80NSSC18K0278. We thank the Tarika family, P. Mahoney, J. Seymour and J. Grancich for logistical support. Thanks to J. Dickson for analytical support. J. Alleon, A. Bahniuk, A. Hayden, C. Howard, H. Grotzinger, S. Jamison-Todd, T. Mahseredjian, K. Metcalfe, D. Morris, I. Overeem, C. Sanders, E. Sibert, M. Tarika, S. O'Reilly, L.A. Riedman and M. Thorpe assisted fieldwork. Thanks also to Jeffrey Dravis, Sam Purkis, Rick Sarg and an anonymous reviewer for their input.

DATA AVAILABILITY STATEMENT

The data that support this work, as well as full resolution base maps and DEMs of Little Ambergris Cay, are available at <https://data.caltech.edu>.

REFERENCES

- Allwood, A.C., Grotzinger, J.P., Knoll, A.H., Burch, I.W., Anderson, M.S., Coleman, M.L. and Kanik, I. (2009) Controls on development and diversity of Early Archean stromatolites. *Proc. Nat. Acad. Sci. USA*, **106**, 9548–9555.
- Andres, M.S. and Reid, R.P. (2006) Growth morphologies of modern marine stromatolites: a case study from Highborne Cay, Bahamas. *Sedimentary Geology*, **185**, 319–328.
- Bontognali, T.R.R., Sessions, A.L., Allwood, A.C., Fischer, W.W., Grotzinger, J.P., Summons, R.E. and Eiler, J.M. (2012) Sulfur isotopes of organic matter preserved in 3.45-billion-year-old stromatolites reveal microbial metabolism. *Proc. Nat. Acad. Sci. USA*, **109**, 15146–15151.
- Demicco, R.V. and Hardie, L.A. (1994) Sedimentary structures and early diagenetic features of shallow marine carbonate deposits. *Atlas 1: SEPM*, 265 p.
- Dill, R.F., Shinn, E.A., Jones, A.T., Kelley, K. and Steinen, R.P. (1986) Giant subtidal stromatolites forming in normal salinity waters. *Nature*, **324**, 55–58.
- Dravis, J.J. (1983) Hardened subtidal stromatolites, Bahamas. *Science*, **219**, 385–386.
- Dravis, J.J. and Wanless, H.R. (2008) Caicos platform models of quaternary carbonate deposition controlled by stronger easterly trade winds – applications to petroleum exploration. *SEPM*, **22**, 171–177.
- Dravis, J.J. and Wanless, H.R. (2017) Impact of strong easterly trade winds on carbonate petroleum exploration – relationships developed from Caicos platform, southeastern Bahamas. *Marine Petrol. Geol.*, **85**, 272–300.
- Dupraz, C. and Visscher, P.T. (2005) Microbial lithification in marine stromatolites and hypersaline mats. *Trends Microbiol.*, **13**, 429–438.
- Dupraz, C., Reid, R.P., Braissant, O., Decho, A.W., Normal, R.S. and Visscher, P.T. (2009) Processes of carbonate precipitation in modern microbial mats. *Earth Sci. Rev.*, **96**, 141–162.
- Fleming, E.D. and Castenholz, R.W. (2007) Effects of periodic desiccation on the synthesis of the UV-screening compound, scytonemin, in cyanobacteria. *Environ. Microbiol.*, **9**, 1448–1455.
- Fleming, K., Johnston, P., Zwart, D., Yokoyama, Y., Lambeck, K. and Chappell, J. (1998) Refining the eustatic sea-level curve since the last glacial maximum using far- and intermediate- field sites. *Earth Planet. Sci. Lett.*, **163**, 327–342.
- Gebelein, C.D. (1969) Distribution, morphology and accretion rate of recent subtidal algal stromatolites, Bermuda. *J. Sediment. Petrol.*, **39**, 49–69.
- Gerdes, G., Klenke, T. and Noffke, N. (2000) Microbial signatures in peritidal siliciclastic sediments: a catalogue. *Sedimentology*, **47**, 279–308.
- Ginsburg, R.N. and Hardie, L.A. (1975) Tidal and storm deposits, northwestern Andros Island, Bahamas. In: *Tidal Deposits* (Ed Ginsburg, R.N.). Springer, Berlin, Heidelberg.
- Ginsburg, R.N., Hardie, L.A., Bricker, O.P., Garrett, P. and Wanless, H.R. (1977) *Exposure Index: A Quantitative Approach to Defining Position Within the Tidal Zone*, Vol. **22**, pp. 7–11. Johns Hopkins Univ. Press, Baltimore, MD.
- Gitelson, A.A., Viña, A., Verma, S.B., Rundquist, D.C., Arkebauer, T.J., Keydan, G., Leavitt, B., Ciganda, V., Burba, G.G. and Suyker, A.E. (2006) Relationship between gross primary production and chlorophyll content in crops: implications for the synoptic monitoring of vegetation productivity. *J. Geophys. Res.: Atmos.*, **111**, 1–13.
- Goehring, L., Conroy, R., Akhter, A., Clegg, W.J. and Routh, A.F. (2010) Evolution of mud-crack patterns during repeated drying cycles. *Soft Matter*, **6**, 2562–2567.
- Golubic, S. (1991) *Microbial Mats of Abu Dhabi. Environmental Evolution, Effects of the Origin and Evolution of Life on Planet Earth*, pp. 103–130. MIT press, Cambridge.
- Gomes, M.L., Riedman, L.A., O'Reilly, S., Lingappa, U., Metcalfe, K., Fike, D.A., Grotzinger, J.P., Fischer, W.W. and Knoll, A.H. (2020) Taphonomy of biosignatures in microbial mats on Little Ambergris Cay, Turks and Caicos Islands. *Front. Earth Sci.*, **8**, 1–22.
- Grotzinger, J.P. (1989) Facies and evolution of Precambrian carbonate depositional systems: emergence of the modern platform archetype. In: *Controls on Carbonate Platforms and Basin Development* (Eds Crevello, P.D., Wilson, J.L., Sarg, F. and Read, J.F.), *SEPM Spec. Publ.*, **44**, 79–106.
- Grotzinger, J.P. and Al-Rawahi, Z. (2014) Depositional facies and platform architecture of microbialite-dominated carbonate reservoirs, Ediacaran-Cambrian Ara Group, Sultanate of Oman. *AAPG Bulletin*, **98**, 1453–1494.
- Grotzinger, J.P. and Knoll, A.H. (1999) Stromatolites in Precambrian carbonates: evolutionary mileposts or environmental dipsticks? *Annu. Rev. Earth Planet. Sci.*, **27**, 313–358.
- Hoffman, P.A. and Grotzinger, J.P. (1993) Orographic precipitation, erosional unloading, and tectonic style. *Geology*, **21**, 195–198.
- Hubas, C., Jesus, B., Passarelli, C. and Jeanton, C. (2011) Tools providing new insight into coastal anoxygenic purple bacterial mats: review and perspectives. *Res. Microbiol.*, **162**, 858–868.
- Jamison-Todd, S., Stein, N., Overeem, I., Khalid, A. and Trower, E.J. (2020) Hurricane deposits on carbonate

- platforms: a case study of Hurricane Irma deposits on Little Ambergris Cay, Turks and Caicos Islands. *J. Geophys. Res. – Earth Surf.*, **125**, 1–16.
- Kerans, C., Zahm, C., Bachtel, S.L., Hearty, P. and Cheng, H.** (2019) Anatomy of a late quaternary carbonate Island: constraints on timing and magnitude of sea-level fluctuations, West Caicos, Turks and Caicos Islands, BWI. *Quatern. Sci. Rev.*, **205**, 193–223.
- Khan, N.S., Ashe, E., Horton, B.P., Dutton, A., Kopp, R.E., Brocard, G., Engelhart, S.E., Hill, D.F., Peltier, W.R., Vane, C.H. and Scatena, F.N.** (2017) Drivers of Holocene sea-level change in the Caribbean. *Quatern. Sci. Rev.*, **155**, 13–36.
- Knoll, A.H.** (2015) Paleobiological perspectives on early microbial evolution. *Cold Spring Harb. Perspect. Biol.*, **7**, 1–17.
- Knoll, A.H., Wörndle, S. and Kah, L.** (2013) Covariance of microfossil assemblages and microbialite textures across a late Mesoproterozoic carbonate platform. *Palaios*, **28**, 453–470.
- Landsea, C.W. and Franklin, J.L.** (2013) Atlantic hurricane database uncertainty and presentation of a new database format. *Mon. Wea. Rev.*, **141**, 3576–3592.
- Lingappa, U.F., Stein, N.T., Metcalfe, K.S., Present, T.M., Orphan, V.J., Grotzinger, J.P., Knoll, A.H., Trower, E.J., Gomes, M.L. and Fischer, W.W.** (2022) Early impacts of climate change on a coastal marine microbial mat ecosystem. *Sci. Adv.*, **8**, eabm7826.
- Logan, B.** (1961) Cryptozoon and associate stromatolites from the recent, Shark Bay, Western Australia. *J. Geology*, **69**, 517–533.
- Maloof, A.C. and Grotzinger, J.P.** (2012) The Holocene shallowing-upward parasequence of north-west Andros Island, Bahamas. *Sedimentology*, **59**, 1375–1407.
- Mangor, K., Drønen, N.K. and Kristensen, N.E.** (2017) *Shoreline Management Guidelines*, 4th edn. DHI Water & Environment, Horsholm.
- Mariotti, G., Pruss, S., Perron, J. and Bosak, T.** (2014) Microbial shaping of sedimentary wrinkle structures. *Nat. Geosci.*, **7**, 736–740.
- Marshall, C.P., Leuko, S., Coyle, C.M., Walter, M.R., Burns, B.P. and Neilan, B.A.** (2007) Carotenoid analysis of halophilic archaea by resonance Raman spectroscopy. *Astrobiology*, **7**, 631–643.
- Martin, J.M., Braga, J.C. and Riding, R.** (1993) Siliciclastic stromatolites and thrombolites, late Miocene, SE Spain. *J. Sediment. Petrol.*, **63**, 131–139.
- Milne, G.A., Long, A.J. and Bassett, S.E.** (2005) Modelling Holocene relative sea-level observations from the Caribbean and South America. *Quatern. Sci. Rev.*, **24**, 1183–1202.
- Neumann, A.C., Gebelein, C.D. and Scoffin, T.P.** (1970) The composition, structure, and erodibility of subtidal mats, Abaco, Bahamas. *J. Sediment. Petrol.*, **40**, 274–297.
- Noffke, N.** (2010) *Geobiology: Microbial Mats in Sandy Deposits from the Archean Era to Today*. Springer-Verlag, Berlin Heidelberg, 166 p.
- Noffke, N., Christian, D., Wacey, D. and Hazen, R.M.** (2013) Microbially induced sedimentary structures recording and ancient ecosystem in the ca. 3.48 billion-year-old Dresser Formation, Pilbara, Western Australia. *Astrobiology*, **13**, 1103–1124.
- Owens, E.H.** (1982) Tombolo. In: *Beaches and Coastal Geology. Encyclopedia of Earth Science*. Springer, Boston, MA. <https://doi.org/10.1007/0-387-30843-1>.
- Pflüger, F. and Gresse, P.G.** (1996) Microbial sand chips – a non-actualistic sedimentary structure. *Sediment. Geol.*, **102**, 263–274.
- Present, T.M., Gomes, M.L., Trower, E.J., Stein, N.T., Lingappa, U.F., Naviaux, J., Thorpe, M.T., Cantine, M.D., Fischer, W.W., Knoll, A.H. and Grotzinger, J.P.** (2021) Non-lithifying microbial ecosystem dissolves peritidal lime sand. *Nat. Commun.*, **12**, 3037.
- Proteau, P.J., Gerwick, W.H., Garcia-Pichel, F. and Castenholz, R.** (1993) The structure of scytonemin, an ultraviolet sunscreen pigment from the sheaths of cyanobacteria. *Experientia*, **49**, 825–829.
- Ranke, E., Reeder, S. and Correa, T.** (2008) Geomorphology and sedimentology of Ambergris ooid shoal, Caicos platform: developing models and analogs for isolated carbonate platforms. *Proceedings Holocene and Pleistocene Carbonates of Caicos Platform, British West Indies, SEPM, Core Workshop*, **22**, 127–132. <https://doi.org/10.2110/pec.08.22.0127>.
- Reid, R.P., Macintyre, I.G., Browne, K.M., Steneck, R.S. and Miller, T.** (1995) Modern marine stromatolites in the Exuma Cays, Bahamas: uncommonly common. *Facies*, **33**, 1–17.
- Reid, R.P., Visscher, P.T., Decho, A.W., Stolz, J.F., Bebout, B.M., Dupraz, C., Macintyre, I.G., Paerl, H.W., Pinckney, J.L., Prufert-Bebout, L., Steppe, T.F. and Des Marais, D.J.** (2000) The role of microbes in accretion, lamination and early lithification of modern marine stromatolites. *Nature*, **406**, 989–992.
- Schieber, J., Bose, P.K., Eriksson, P.G., Banerjee, S., Sarkar, S., Altermann, W. and Catuneau, O.** (2007) *Atlases in Geoscience*. Elsevier, Amsterdam, the Netherlands. 307 p.
- Schopf, J.W.** (2006) Fossil evidence of Archaean life. *Philos. Trans. R. Soc. Long. B. Biol. Sci.*, **361**, 869–885.
- Scoffin, T.P.** (1970) The trapping and binding of subtidal carbonate sediments by marine vegetation in Bimini lagoon, Bahamas. *J. Sed. Res.*, **40**, 249–273.
- Semikhatov, M.A., Gebelein, C.D., Cloud, P., Awramik, S.M. and Benmore, W.C.** (1979) Stromatolite morphogenesis – progress and problems. *Can. J. Earth Sci.*, **16**, 992–1015.
- Shepard, R.N. and Sumner, D.Y.** (2010) Undirected motility of filamentous cyanobacteria produces reticulate mats. *Geobiology*, **8**, 179–190.
- Soltz, J.F.** (2000) Structure of microbial mats and biofilms. In: *Microbial Sediments*. Springer, Berlin, Heidelberg. https://doi.org/10.1007/978-3-662-04036-2_1.
- Stuiver, M. and Polach, H.A.** (1977) Discussion reporting of ¹⁴C data. *Am. J. Sci.*, **19**, 355–363.
- Toscano, M.A. and Macintyre, I.G.** (2003) Corrected western Atlantic Sea-level curve for the last 11,000 years based on calibrated ¹⁴C dates from *Acropora palmata* framework and intertidal mangrove peat. *Coral Reefs*, **22**, 257–270.
- Trembath-Reichert, E., Ward, L.M., Slotznick, S.P., Bachtel, S.L., Kerans, C., Grotzinger, J.P. and Fischer, W.W.** (2016) Gene sequencing-based analysis of microbial-mat morphotypes, Caicos platform, British West Indies. *J. Sediment. Res.*, **86**, 629–636.
- Trower, E.J., Cantine, M.D., Gomes, M.L., Grotzinger, J.P., Knoll, A.H., Lamb, M.P., Lingappa, U., O'Reilly, S.S., Present, T.M., Stein, N., Strauss, J.V. and Fischer, W.W.** (2018) Active ooid growth driven by sediment transport in a high-energy shoal, Little Ambergris Cay, Turks and Caicos Islands. *J. Sediment. Res.*, **88**, 1132–1151.
- Trower, L., Mahseredjian, T., Overeem, I., Gomes, M., Howard, C., Lingappa, U.F., Present, T. and Sibert, E.C.** (2019) Grain-trapping by microbial mats – a key mechanism of sediment accumulation in mangroves? *AGU Annual Meeting*. EP23B-03.

- Van Gernerden, H.** (1993) Microbial mats: A joint venture. *Mar. Geol.*, **113**, 3–25.
- Visscher, P.T., Reid, R.P., Bebout, B.M., Hoefl, S.E., Macintyre, I.G. and Thompson, J.A.** (1998) Formation of lithified micritic laminae in modern marine stromatolites (Bahamas): the role of sulfur cycling. *Am. Mineral.*, **83**, 1482–1493.
- Walter, M.R., Goode, A.D.T. and Hall, W.D.M.** (1976) Microfossils from a newly discovered Precambrian stromatolitic iron formation in Western Australia. *Nature*, **261**, 221–223.
- Wanless, H.R. and Dravis, J.** (2008) Role of storms and prevailing energy in defining sediment body geometry, composition, and texture on Caicos platform: developing models and analogs for isolated carbonate platforms: Holocene and Pleistocene carbonates of Caicos platform, British West Indies. *SEPM, Core Workshop Notes*, 22 <https://doi.org/10.2110/pec.08.22.0013>.
- Wanless, H.R., Tyrrell, J.M., Tedesco, L.P. and Dravis, J.J.** (1988) Tidal-flat sedimentation from Hurricane Kate, Caicos platform, British West Indies. *J. Sediment. Petrol.*, **58**, 724–738.
- Wanless, H.R., Dravis, J.J., Tedesco, L.P. and Rossinsky, V., Jr.** (1989) Carbonate environments and sequences of Caicos platform: Caicos, British West Indies to Miami, Florida. *AGU Field Trip Guidebook*, 374 <https://doi.org/10.1029/FT374>.
- Wu, M., Harris, P., Eberli, G. and Purkis, S.J.** (2021) Sea-level, storms, and sedimentation – controls on the architecture of the Andros tidal flats (Great Bahama Bank). *Sediment. Geol.*, **420**, 105932.

Manuscript received 7 February 2023; revision accepted 28 March 2023